Journal of Petroleum Science and Engineering 214 (2022) 110518

Contents lists available at ScienceDirect

Journal of Petroleum Science and Engineering

journal homepage: www.elsevier.com/locate/petrol

An XFEM-based approach for 3D hydraulic fracturing simulation considering crack front segmentation

Fang Shi [a,*], Daobing Wang [b], Hong Li [c]

[a] Jiangsu Key Laboratory of Advanced Manufacturing Technology, Huaiyin Institute of Technology, Huai'an, Jiangsu, 223003, China
[b] School of Mechanical Engineering, Beijing Key Laboratory of Pipeline Critical Technology and Equipment for Deep Water Oil & Gas Development, Beijing Institute of Petrochemical Technology, Beijing, 102617, China
[c] Faculty of Mechanical & Material Engineering, Huaiyin Institute of Technology, Huai'an, Jiangsu, 223003, China

ARTICLE INFO

Keywords:
Hydraulic fracturing simulation
Extended finite element method
Local mesh refinement
Crack front segmentation

ABSTRACT

Hydraulic fracturing is a commonly adopted and effective well stimulation technique in the oil and gas extraction area. Under a mixed I/III loading condition, the crack front segmentation (i.e., the parent crack segments into echelon-shaped daughter cracks) usually occurs, which highly complicates the paths of fluid-driven cracks. This paper presents an efficient numerical model for 3D hydraulic fracturing simulation considering crack front segmentation on basis of the extended finite element method (XFEM). Solutions of the momentum balance equation and the fluid flow equation are simultaneously determined by the Newton-Raphson method along with a reduction technique. In the XFEM framework, a robust local mesh-refinement scheme of the tip-enriched elements is designed to enhance the resolution of the near-front stress field which is crucial for the determination of crack segmentation and propagation behaviors. The locally refined tip-enriched elements are then divided into a series of tetrahedra to perform high-accuracy numerical integration. After verification of the proposed approach, the effects of several critical parameters in hydraulic fracturing treatments are investigated. Results show that crack front segmentation has significant effects on the resulting crack paths and crack aperture distribution. The propagation of hydraulic fractures will be depressed on account of the stress shadow induced by overlapped segments, leading to higher pumping pressure compared to the case without considering front segmentation. The sensitivity analyses indicate that larger elastic modulus of rock formation, larger fluid viscosity, higher fluid pumping rate, and smaller fluid leak-off coefficient can alleviate the influence of crack front segmentation on the pumping pressure. Larger elastic modulus, larger fluid viscosity, higher fluid pumping rate, and greater fluid leak-off coefficient lead to smaller twisting angles of the segments and smaller overlapping ratios.

1. Introduction

In the energy extraction field, hydraulic fracturing is an effective well stimulation technique that fractures the rock formation by a pressured fluid containing proppant to form unobstructed flow paths for oil or natural gas, and thus to improve oil-gas production. Since the first hydraulic fracturing test in 1947 conducted by the Stanolind Oil and Gas Company at the Hugoton gas field (Montgomery and Smith, 2010), millions of hydraulic fracturing jobs have been successfully performed worldwide, resulting in a substantial increase in the supply of global oil and gas resources. However, hydraulic fracturing is a very complicated process (Jamaloei, 2021) composed of several intercoupling physical sub-processes such as the deformation of bedrock formations, fluid flow in the fracture, fracture propagation, proppant transport, fluid leak-off, and interaction between fluid-driven and natural fractures. Besides, field data and experimental studies indicate that real hydro-fractures propagate in a complex three-dimensional (3D) manner under the influence of non-uniform in-situ stresses (Adachi et al., 2007). It is therefore of great interest to investigate the mechanism of 3D hydraulic fracturing and study the effects of key parameters including elastic modulus of rock formation, fluid viscosity, pumping rate, and leak-off coefficient on crack paths.

It has been widely observed (Knauss, 1970; Pham and Ravi-Chandar, 2016; Pons and Karma, 2010; Sommer, 1969) that a crack in mixed I/III or I/II/III modes will frequently twist and split into a series of daughter cracks (Fig. 1) which gradually grow towards the mode-I direction

* Corresponding author.
E-mail address: shifang@hyit.edu.cn (F. Shi).

https://doi.org/10.1016/j.petrol.2022.110518
Received 26 February 2022; Received in revised form 13 April 2022; Accepted 15 April 2022
Available online 20 April 2022

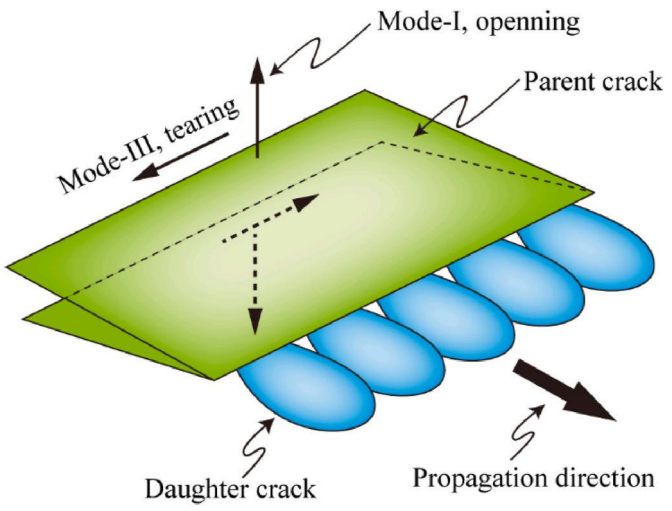

Fig. 1. Depiction of the crack front segmentation phenomenon. Several echelon-shaped daughter cracks are formed along the front of the parent crack in the mixed-mode I-III loading condition. Experimental observations (Lazarus et al., 2001; Pham and Ravi-Chandar, 2016) indicate that daughter cracks are of a similar size, in an almost perfect periodic pattern with similar distance, and oriented with similar angles, as shown in this figure.

during the following propagation process. This kind of phenomenon is usually called crack front segmentation (or fragmentation) and has been clearly evidenced in both nature and laboratory experiments performed in different kinds of engineering and geological materials (Fig. 2). Some attention has been paid to the mechanisms that govern the initiation and progression of daughter cracks along the parent crack periphery. According to experimental data of Homalite-100 specimens, Lin et al. (2010) found a correlation between crack twisting angle and segments spacing. Based on a theoretical model in the context of linear elastic fracture mechanics (LEFM), Leblond et al. (2011) suggested that the unstable propagation will be triggered when the stress intensity factor ratio K_{III}/K_I exceeds a Poisson's ratio related threshold. More recently, Leblond and Frelat (2014) proposed an expression giving the tilled angle of daughter crack as a function of K_{III}/K_I. Chen et al. (2015) systematically studied the facet coarsening process (i.e., increase of facet width and facet spacing during propagation) of daughter cracks and revealed its self-similar property. After performing a series of laboratory experiments, Pham and Ravi-Chandar (2016) identified a sequence of events to illustrate the crack front fragmentation process: the nucleation of daughter cracks, the arrest of some daughter cracks caused by facet interactions, and the possible further propagation of the parent crack. In addition to experimental and theoretical research, the phase-field method (PFM) (Biner, 2017) has been used by some researchers to simulate the crack front segmentation process. For example, Pons and Karma (2010) performed large-scale PFM simulations and compared the facet twist angle with experimental observation as well as theoretical prediction. Henry (2016) investigated the crack front fragmentation process under mixed loading conditions using the PFM and observed propagation patterns similar to experimental findings. Pham and Ravi-Chandar (2017) successfully modeled the formation procedure of echelon cracks by introducing initial defects to trigger front segmentation in their PFM model. Although the PFM has successfully replicated the crack front segmentation process, the drawback of extremely large computational costs (Henry, 2016; Pons and Karma, 2010) limits its application in large-scale engineering problems, for instance, hydraulic fracturing simulation.

Because of the limitations and narrow application scopes of theoretical models (Adachi et al., 2007) (i.e., PKN model, KGD model, radial model, pseudo-3D model, etc), simulations of hydraulic fracturing have been broadly performed by adopting different kinds of numerical methods, such as the finite element method (FEM) (Advani and Lee, 1982), the discrete element method (DEM) (Damjanac and Cundall, 2016), the phase-field model (Guo et al., 2018), the boundary element method (BEM) (Dong and Pater, 2001), the peridynamics approach (Ouchi et al., 2015), the smeared crack approach (Ji et al., 2009), the virtual internal bond (VIB) method (Huang et al., 2013), the XFEM (Shi et al., 2021; Wang et al., 2021), etc. However, there exists scant literature in the context of front segmentation of fluid-driven cracks. Based on a multidimensional VIB model, the phenomenon of crack front segmentation of hydraulic fractures in brittle rock was observed in the simulations performed by Huang et al. (2013). Fu and Bunger (2019) also noticed the splitting of crack front in their DEM-based hydraulic fracturing simulation. Since its first report in 1999 (Belytschko and Black, 1999; Moës et al., 1999), the XFEM has emerged as a powerful numerical method for crack propagation simulation due to its dominant feature of mesh independence. By introducing additional degrees of freedom (DOFs) governed by enrichment functions related to the asymptotic features of the displacement field, the remeshing procedure can be effectively avoided. For example, Haddad and Sepehrnoori (2016) performed 3D hydraulic fracturing simulations utilizing the XFEM-based cohesive zone model in the Abaqus software package. Paul et al. (2018) presented a numerical model to simulate the propagation of

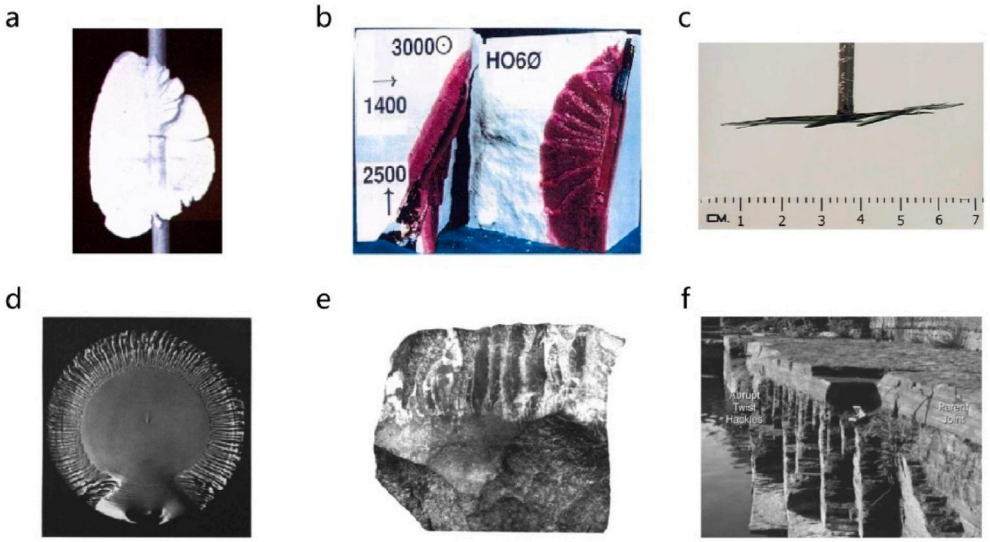

Fig. 2. Segmented cracks recorded in experiments ((a) to (d)) and in nature ((e) and (f)). (a) Segmented hydraulic crack along a borehole inside a specimen made of ordinary gelatin (Hubbert and Willis, 1957); (b) Segmented hydro-fracture emerged from the wellbore in hydrostone block experiment (Abass et al., 1996); (c) Side view of a branched hydraulic crack at the end of a laboratory-scale borehole in a PMMA specimen (Wu et al., 2009); (d) Lance-shaped facets formed along the periphery of a mixed I-III mode crack inside a glass specimen (Sommer, 1969); (e) Natural echelon cracks (the top half) and its parent crack (the bottom half) discovered in a shale sample (Pollard et al., 1982); and (f) Natural tilted facets found in shale in Taughannock Falls State Park, New York (Younes and Engelder, 1999).

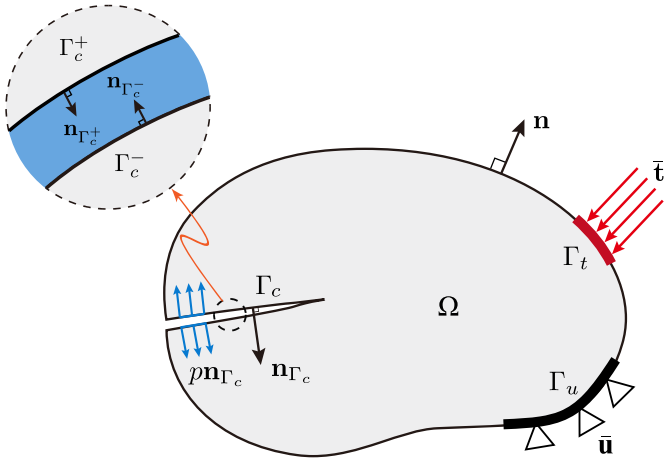

Fig. 3. Schematic of a hydraulic fracture in a 3D domain.

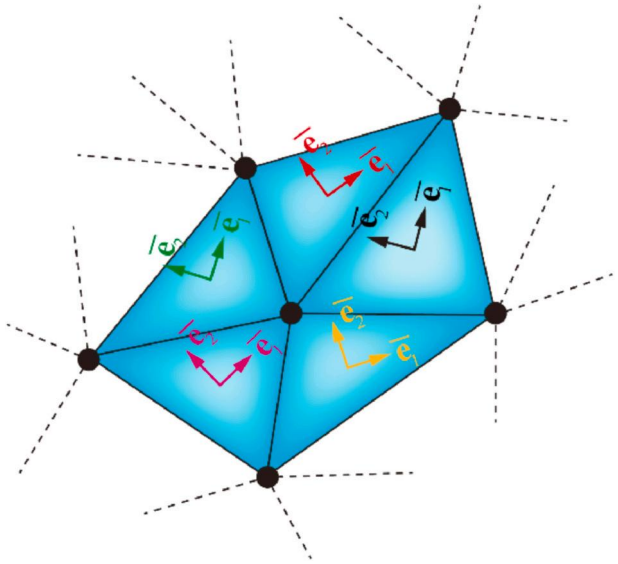

Fig. 4. Illustration of fluid elements and corresponding local coordinate systems. Each fluid element is composed of three fluid nodes denoted by black dots. The base vector $\bar{\mathbf{e}}_1$ of the local coordinate system points to the first fluid node and $\bar{\mathbf{e}}_1 \times \bar{\mathbf{e}}_2 = \mathbf{n}_{\Gamma_c}$.

3D non-planar fluid-driven cracks in poroelastic saturated media. Gupta and Duarte (2018) established a coupled numerical model to perform hydraulic fracturing simulation of 3D cracks using the generalized finite element method (GFEM), a method similar to the XFEM. Due to the existence of tectonic faults, joints or other geological discontinuities, material heterogeneity of rock formation, misalignment of perforations, and the effects of stress shadow, the hydraulic fractures usually undergo mixed loading conditions with mode III component, and thus resulting in complex crack geometry with echelon cracks or tilted facets after branching (Abass et al., 1996; Abelson and Agnon, 1997; Hubbert and Willis, 1957). Nevertheless, when it comes to hydraulic fracturing simulation, intact cracks without branching or segmentation are assumed by researchers in almost all available literature (Jamaloei, 2021; Lecampion et al., 2018) on account of the geometrical complexity of the unstable mixed-mode fracture. Recently, Wu et al. (2009) performed a laboratory-scale hydraulic fracturing experimental study using polymethyl methacrylate (PMMA) and concluded that ignoring crack front segmentation phenomenon might severely underestimate the net pressure and thus leading to unreliable results. Consequently, there is an urgent need to establish effective numerical models capable of dealing with this kind of segmentation problems.

In the following, the governing equations and discretization will be given in Section 2. To increase the simulation accuracy and the capability of the proposed model to deal with the complex phenomenon of echelon cracks formation, some computational issues including the local mesh refinement strategy of the tip-enriched elements, fitting of crack front vertices, and partition and integration of enriched elements, and the crack propagation criterion will be presented in Section 3. Verification of the proposed numerical model will be performed in Section 4, followed by the parameter sensitivity analysis given in Section 5.

2. Coupled governing equations

2.1. Momentum balance equation

As depicted in Fig. 3, consider a quasi-static crack Γ_c in a 3D rock formation Ω which follows a linear elastic constitutive relation $\boldsymbol{\sigma} = \mathbf{D} : \boldsymbol{\varepsilon}$, in which $\boldsymbol{\sigma}$, $\boldsymbol{\varepsilon}$, and $\mathbf{D}$ represent the Cauchy stress tensor, the strain tensor for small deformation, and the elastic tensor depending on the elastic modulus E and Poisson's ratio υ, respectively. The boundary Γ of Ω is made up of four parts: Γ_t with externally applied stress $\bar{\mathbf{t}}$, the interior boundary (i.e., the crack surface) $\Gamma_c = \Gamma_c^+ \cup \Gamma_c^-$ with fluid pressure p, Γ_u with imposed displacement field $\bar{\mathbf{u}}$, and the remaining part of Γ. Without considering the body force, the momentum balance equation and its associated boundary conditions can be written as

$$\begin{cases} \nabla\cdot\boldsymbol{\sigma} = 0 \quad in \quad \Omega \\ \mathbf{u} = \bar{\mathbf{u}} \quad on \quad \Gamma_u \\ \boldsymbol{\sigma}\cdot\mathbf{n}_{\Gamma_t} = \bar{\mathbf{t}} \quad on \quad \Gamma_t \\ \boldsymbol{\sigma}\cdot\mathbf{n}_{\Gamma_c} = p\mathbf{n}_{\Gamma_c} \quad on \quad \Gamma_c \end{cases} \tag{1}$$

where $\mathbf{n}_\Gamma$ represents the outwards normal vector of boundary Γ.

2.2. Fluid flow and leak-off inside the fracture

In this paper, the fluid lag between the front of the incompressible and Newtonian fluid and the crack front is neglected. During hydraulic fracture treatment, the laminar flow which can be described using Poiseuille's law (Adachi et al., 2007) along with the mass conservation law is the main flow regime inside the cracks. For the fluid elements with three fluid nodes shown in Fig. 4, $\{\bar{\mathbf{e}}_1, \quad \bar{\mathbf{e}}_2\}$ are base vectors of the local coordinate system attached to the element center. For a point $\bar{\mathbf{x}} = (\bar{x}_1, \bar{x}_2)$ in the fluid element, the fracture width w is directly related to fluid pressure gradient and fluid viscosity μ (Batchelor, 1967):

$$\frac{\partial w}{\partial t} - \nabla_{\bar{\mathbf{x}}}\left(\frac{w^3}{12\mu}\nabla_{\bar{\mathbf{x}}} p\right) + Q_L = Q_I \tag{2}$$

where t denotes time, Q_I is the fluid injection rate per unit area, Q_L is the fluid leak-off rate to the rock formation per unit area, and $\nabla_{\bar{\mathbf{x}}}$ represents the gradient operator:

$$\nabla_{\bar{\mathbf{x}}} = \frac{\partial}{\partial \bar{x}_1}\bar{\mathbf{e}}_1 + \frac{\partial}{\partial \bar{x}_2}\bar{\mathbf{e}}_2 \tag{3}$$

Q_L can be described by Carter's model (Carter, 1957):

$$Q_L = \frac{2C_L}{\sqrt{t - t_0(\bar{\mathbf{x}})}} \tag{4}$$

in which C_L represents Carter's leak-off coefficient, and t_0 denotes the time when the crack front first reaches the point $\bar{\mathbf{x}}$. In addition to the fluid injection rate Q_{inj} at the crack mouse, additional boundary condition and solvability condition of Eq. (2) are the zero flux applied at the crack tip (Jin and Arson, 2020) and the global mass conservation law (Adachi et al., 2007):

$$Q_{inj} = \int_{\Gamma_c} \dot{w} d\Gamma + \int_{\Gamma_c} Q_L d\Gamma \tag{5}$$

2.3. Weak forms

We can obtain the weak formulation of the momentum balance equation by introducing the virtual displacement $\delta\mathbf{u}(\mathbf{x},t)$, integrating by parts, and then employing the divergence theorem:

$$\int_{\Omega}\nabla\delta\mathbf{u}:\boldsymbol{\sigma}d\Omega+\int_{\Gamma_c}[[\delta\mathbf{u}]]\cdot p\mathbf{n}_{\Gamma_c}d\Gamma=\int_{\Gamma_t}\delta\mathbf{u}\cdot\bar{\mathbf{t}}d\Gamma \tag{6}$$

in which $[[\delta\mathbf{u}]]=\delta\mathbf{u}(\Gamma_c^+)-\delta\mathbf{u}(\Gamma_c^-)$. By multiplying the test function $\delta p(\bar{\mathbf{x}},t)$ and integrating by parts, the weak form of the fluid flow equation (Eq. (2)) can be derived as:

$$\int_{\Gamma_c}\frac{w^3}{12\mu}\nabla_{\bar{\mathbf{x}}}\delta p\cdot\nabla_{\bar{\mathbf{x}}}pd\Gamma=\int_{\Gamma_c}\delta p\left(Q_I-Q_L-\frac{\partial w}{\partial t}\right)d\Gamma \tag{7}$$

2.4. Discretization and solution strategy

The displacement field $\mathbf{u}(\mathbf{x})$ is discretized using the XFEM in which the Heaviside enrichment function $H(\mathbf{x})$ and crack tip enrichment functions $F_l(\mathbf{x})\quad(l=1,\cdots,4)$ are adopted, respectively, to depict the displacement jump across the crack surface and the singular displacement field near the crack front (Moës et al., 1999):

$$\mathbf{u}(\mathbf{x})=\sum_{I\in S_{all}}N_I^u(\mathbf{x})\mathbf{u}_I+\sum_{I\in S_H}N_I^u(\mathbf{x})H(\mathbf{x})\mathbf{a}_I+\sum_{I\in S_{tip}}N_I^u(\mathbf{x})\sum_{l=1}^{4}F_l(\mathbf{x})\mathbf{b}_I^l \tag{8}$$

In the above, S_{all}, S_H, and S_{tip} represent respectively the set of all nodes, the set of Heaviside enriched nodes, and the set of tip-enriched nodes, respectively; $\mathbf{u}_I$, $\mathbf{a}_I$, and $\mathbf{b}_I^l$ denote the vectors of DOFs of S_{all}, S_H, and S_{tip}; N_I^u is the standard shape function. $H(\mathbf{x})$ takes the following form (Moës et al., 1999):

$$H(\mathbf{x})=\begin{cases}1 & if\quad(\mathbf{x}-\mathbf{x}^*)\cdot\mathbf{n}_{\Gamma_c}\geq 0\\ -1 & otherwise\end{cases} \tag{9}$$

where $\mathbf{x}^*$ represents the closest point on the crack to point $\mathbf{x}$. Functions $F_l(\mathbf{x})$ can be written as (Moës et al., 2002):

$$\{F_l(r,\theta)\}_{l=1,\ldots,4}=\left\{\sqrt{r}\sin\frac{\theta}{2},\sqrt{r}\cos\frac{\theta}{2},\sqrt{r}\sin\theta\sin\frac{\theta}{2},\sqrt{r}\sin\theta\cos\frac{\theta}{2}\right\} \tag{10}$$

in which r and θ represent the polar coordinates of the cylindrical coordinate system locally defined at the crack front (Moës et al., 2002; Shi and Liu, 2021).

Due to the loss of partition of unity feature (Melenk and Babuška, 1996), the enrichment functions $\psi(\mathbf{x})$ of blending elements (i.e., elements whose nodes are partially enriched) require special treatment:

$$\psi^{\mathrm{mod}}(\mathbf{x})=\psi(\mathbf{x})R(\mathbf{x}) \tag{11}$$

where $R(x)$ is the ramp function proposed by Fries (2008).

$$R(\mathbf{x})=\sum_{I\in S_{enrich}}N_I^u(\mathbf{x}) \tag{12}$$

with S_{enrich} denoting the set of enriched nodes. Thus, for blending elements, their displacements can be written as

$$\mathbf{u}(\mathbf{x})=\sum_{I\in S_{all}}N_I^u(\mathbf{x})\mathbf{u}_I+\sum_{\alpha=1}^{NE}\sum_{I\in M_{enrich}}N_I^u(\mathbf{x})\psi_\alpha^{\mathrm{mod}}(\mathbf{x})\mathbf{c}_I^\alpha \tag{13}$$

in which M_{enrich} represents the nodes-set composed of enriched nodes of enriched elements and other conventional nodes of blending elements, $\mathbf{c}_I$ is corresponding vectors of DOFs, and NE is the number of enrichment functions of blending elements.

Substitution of Eq. (8) or Eq. (13) into Eq. (6) yields the discretization form as (Shi et al., 2017):

$$\mathbf{KU}-\mathbf{QP}-\mathbf{F}^{\mathrm{ext}}=0 \tag{14}$$

where $\mathbf{K}$, $\mathbf{F}^{\mathrm{ext}}$, $\mathbf{U}$, $\mathbf{P}$, $\mathbf{Q}$ denote respectively the matrix of global stiffness, the vector of global external force, the vector of displacement of all DOFs including enriched ones, the vector of pressure of all fluid nodes, and the coupling matrix which converts the fluid pressure to equivalent nodal forces applied on the crack surface:

$$\mathbf{Q}=\int_{\Gamma_c}(\mathbf{N}^w)^T\mathbf{n}_{\Gamma_c}\mathbf{N}^p d\Gamma \tag{15}$$

in which $\mathbf{N}^w$ is the shape function matrix used to transform the displacement $\mathbf{U}$ to the crack width vector $\mathbf{w}$, and $\mathbf{N}^p$ denotes the shape function matrix of fluid elements. In Eq. (14), $\mathbf{K}$ can be divided into four parts in accordance with the standard and enriched DOFs:

$$\mathbf{K}=\begin{bmatrix}\int_{\Omega}(\mathbf{B}^{std})^T\mathbf{D}\mathbf{B}^{std}d\Omega & \int_{\Omega}(\mathbf{B}^{std})^T\mathbf{D}\mathbf{B}^{enr}d\Omega\\ \int_{\Omega}(\mathbf{B}^{enr})^T\mathbf{D}\mathbf{B}^{std}d\Omega & \int_{\Omega}(\mathbf{B}^{enr})^T\mathbf{D}\mathbf{B}^{enr}d\Omega\end{bmatrix}=\begin{bmatrix}\mathbf{K}_{ss} & \mathbf{K}_{se}\\ \mathbf{K}_{es} & \mathbf{K}_{ee}\end{bmatrix} \tag{16}$$

where the superscripts *std* and *enr* are short for "standard" and "enriched", respectively; and $\mathbf{B}$ represents the strain-displacement matrix.

The solid domain is meshed with linear hexahedral elements with eight nodes. The standard elements without enrichment and blending elements are integrated with $2\times2\times2$ and $6\times6\times6$ Gauss points, respectively. For the fully enriched elements, however, the numerical integration is implemented using 4 Gauss points within the tetrahedra obtained after performing element subdivision (Loehnert et al., 2011). Details on the numerical integration procedure can be found in our previous work (Shi and Liu, 2021) except for the partitioning process of enriched elements that contain segmentation points (or called fragmentation points), which will be detailed in Section 3.2.

The fluid pressure of point $\bar{\mathbf{x}}$ is computed as:

$$p(\bar{\mathbf{x}})=\sum_{I\in S_{fluid}}N_I^p(\bar{\mathbf{x}})p_I \tag{17}$$

In the above, S_{fluid}, p_I, and N_I^p denote the set of fluid nodes, the nodal fluid pressure, and the shape function of fluid elements, respectively. Details on the identification of fluid nodes and elements based on an explicit crack surface description scheme are referred to our recent paper (Shi and Liu, 2021). Then, the discrete form of Eq. (7) can be written as (Shi et al., 2017)

$$\mathbf{Q}^T\dot{\mathbf{U}}+\mathbf{HP}+\mathbf{S}-\mathbf{G}=0 \tag{18}$$

where the dot denotes time derivative; $\mathbf{H}$, $\mathbf{S}$, and $\mathbf{G}$ are the flow matrix, the vector of source term, and the vector of leak-off term, respectively:

$$\mathbf{H}=\int_{\Gamma_c}\frac{w^3}{12\mu}\left(\nabla_{\bar{\mathbf{x}}}{}^T\mathbf{N}^p\right)\left(\nabla_{\bar{\mathbf{x}}}\mathbf{N}^p\right)d\Gamma \tag{19}$$

$$\mathbf{S}=\int_{\Gamma_c}(\mathbf{N}^p)^TQ_I d\Gamma \tag{20}$$

$$\mathbf{G}=\int_{\Gamma_c}(\mathbf{N}^p)^TQ_L d\Gamma \tag{21}$$

The implicit backward Euler method is adopted to perform the discretization in time of Eq. (18). For each time step, the coupling equations (Eq. (14) and (18)) are solved using the Newton-Raphson (N-R) method. The total computational cost can be decreased by removing the conventional DOFs during the N-R iteration process by virtue of the reduction technique (Shi et al., 2017). The reduced residual vector $\mathbf{R}_R^i$ (subscript R is short for "Reduced") and the corresponding reduced

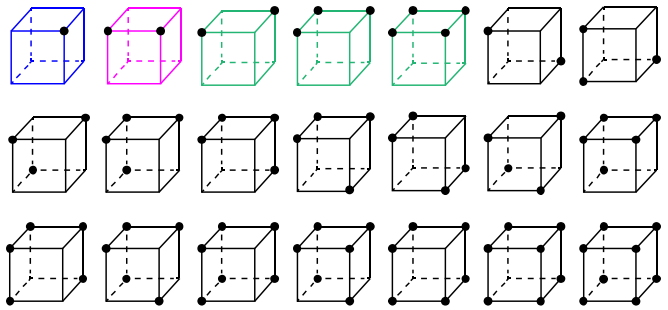

Fig. 5. Illustration of all 21 possible combinations of enriched nodes of the standard linear 8-noded hexahedral element. The enriched nodes are denoted by black dots. The combinations are classified into four categories colored in blue, fuchsia, green, and black, respectively. (For interpretation of the references to color in this figure legend, the reader is referred to the Web version of this article.)

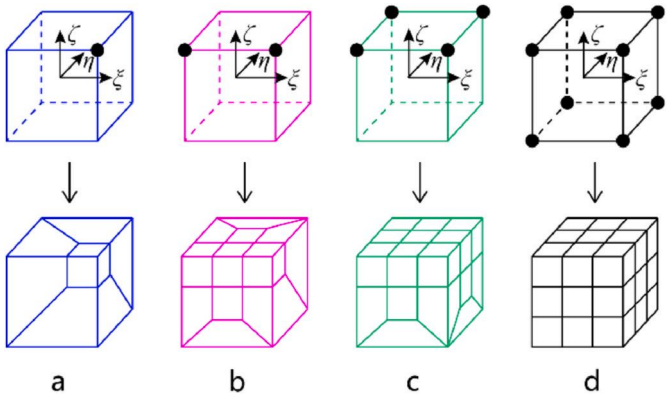

Fig. 6. Illustration of refinement templates of enriched elements shown in Fig. 5. The enriched nodes are denoted by black dots. (ξ, η, ζ) shown in this figure denote natural coordinate systems.

Jacobin matrix $\mathbf{J}_R^i$ of N-R iteration step i can be written as, respectively:

$$\mathbf{R}_R^i = \begin{bmatrix} 0 & 0 \\ -\mathbf{Q}_e^T & 0 \end{bmatrix} \begin{pmatrix} \Delta\mathbf{U}_e \\ \Delta\mathbf{P} \end{pmatrix}^i + \begin{bmatrix} \mathbf{K}_{ee} - \mathbf{K}_{es}\mathbf{K}_{ss}^{-1}\mathbf{K}_{se} & -\mathbf{Q}_e \\ 0 & -\Delta t\mathbf{H}^i \end{bmatrix} \begin{pmatrix} \mathbf{U}_e \\ \mathbf{P} \end{pmatrix}^i - \begin{pmatrix} -\mathbf{K}_{es}\mathbf{K}_{ss}^{-1}\mathbf{F}_s^{\text{ext}} \\ \Delta t\mathbf{S}^i - \Delta t\mathbf{G}^i \end{pmatrix}^i \tag{22}$$

$$\mathbf{J}_R^i = \begin{bmatrix} \mathbf{K}_{ee} - \mathbf{K}_{es}\mathbf{K}_{ss}^{-1}\mathbf{K}_{se} & -\mathbf{Q}_e \\ -\mathbf{Q}_e^T & -\Delta t\mathbf{H}^i \end{bmatrix} \tag{23}$$

where $\mathbf{Q}_e$ is the submatrix of $\mathbf{Q}$ after deleting the terms related to standard DOFs, $\mathbf{U}_e$ represents the vector of enriched DOFs, and $\mathbf{F}_s^{\text{ext}}$ is the subvector of $\mathbf{F}^{\text{ext}}$ after deleting enriched DOFs related terms. In this study, the reduced Jacobin matrix $\mathbf{J}_R^i$ is assembled in an element-by-element way (Smith et al., 2014) to eliminate the need to explicitly form the global matrix and reduce the total memory footprint which can be significantly large for a field-scale hydraulic fracturing simulation.

The increments of the N-R iteration $\Delta\widehat{\mathbf{U}} = \{\Delta\mathbf{U}_e, \Delta\mathbf{P}\}^T$ can be obtained by solving the following linear system:

$$\mathbf{J}_R^i \Delta\widehat{\mathbf{U}}^i = \mathbf{R}_R^i \tag{24}$$

Finally, the displacement and fluid pressure fields are synchronously updated according to $\widehat{\mathbf{U}}^{i+1} = \widehat{\mathbf{U}}^i - \Delta\widehat{\mathbf{U}}^i$ until the solution converges:

$$\frac{\left\|\Delta\widehat{\mathbf{U}}^i - \Delta\widehat{\mathbf{U}}^{i-1}\right\|}{\left\|\Delta\widehat{\mathbf{U}}^{i-1}\right\|} \le \varepsilon_{\text{tol}} \tag{25}$$

in which $\|\|$ denotes L_2 norm operator and the convergence tolerance ε_{tol} is chosen to be 10^{-6}.

3. Computational implementation issues

Before diving into the implementation details of the proposed numerical method, considering the extreme complexity of the crack front fragmentation phenomenon, the following assumptions are given to make the problem numerically solvable. In this paper, only the first-order segments produced from the periphery of parent crack are simulated, and the second-order segments (Wu et al., 2009) produced from the daughter cracks will not be considered. The process of neighboring facets merging (i.e., facet coarsening) (Chen et al., 2015) is ignored in this study. Besides, the number of segments emerged along the crack periphery depends on the material property, crack geometry, external loading, and initial defects in a complicated way and seems to be intractable to be numerically decided (Meng and Pollard, 2012; Pham and Ravi-Chandar, 2014, 2017). Hence, in this paper, the number of segments is pre-specified.

3.1. Local mesh refinement of tip-enriched elements

Because of the intrinsic complexity of the segmentation phenomenon, a high-resolution stress field must be made available before determining the direction and length of crack growth. To this end, a mesh refinement approach is implemented entirely within the framework of the XFEM. In order to restrain the number of added DOFs, the proposed approach only refines enriched elements containing tip-enriched nodes. Another advantage of performing mesh refinement is that it can eliminate the potential inconsistency between different enrichment functions, for example, between enrichment functions $H(\mathbf{x})$ and $F_l(\mathbf{x})$ in elements with kinking crack surface (Belytschko and Black, 1999). Furthermore, this approach is quite simple to be implemented in existing XFEM codes.

As shown in Fig. 5, there exist 21 potential combinations of enriched nodes for a hexahedral element. Four distinct refinement templates depicted in Fig. 6 are respectively used to divide the blue, fuchsia, green, and black elements shown in Fig. 5 according to the following general rules: an element edge with a single enriched node is divided into two parts by inserting an additional node at the trisection point near the enriched node; an element edge with two enriched nodes is equally divided into three parts by inserting two additional nodes at trisection points. It can be noticed that templets (a), (b), (c), and (d) are point, edge, face, and volume refinement templates and form 4, 11, 22, and 27 elements after refinement, respectively. Following the proposed rules, the conformity (Lo, 2015; Sun et al., 2012) of the refined mesh can be maintained.

The subdividing of refinement templates (a) and (d) is fairly simple. Templates (b) and (c) should be given more consideration. For templates (b) and (c) shown in Figs. 7 and 8, the coordinates of inserted nodes (nodes 1 to 6 for template (b), nodes 1 to 8 for template (c)) are listed in Table 1. In this way, we can make sure that the grey resultant faces illustrated in Fig. 8a are all planar and all refined elements are hexahedral, thus the mesh conformity can be guaranteed. It is important to note that when ordering the added nodes to construct hexahedral elements, it is critical to ensure that the determinant of the Jacobian is positive to avoid unreasonable element stiffness matrix. A flexible Fortran code for performing the refinement procedure outlined in this paper has been uploaded to GitHub: https://github.com/PhiPsi-Software/local_mesh_refinement, from which the robust and complete implementation of all templates can be accessed. After performing the local

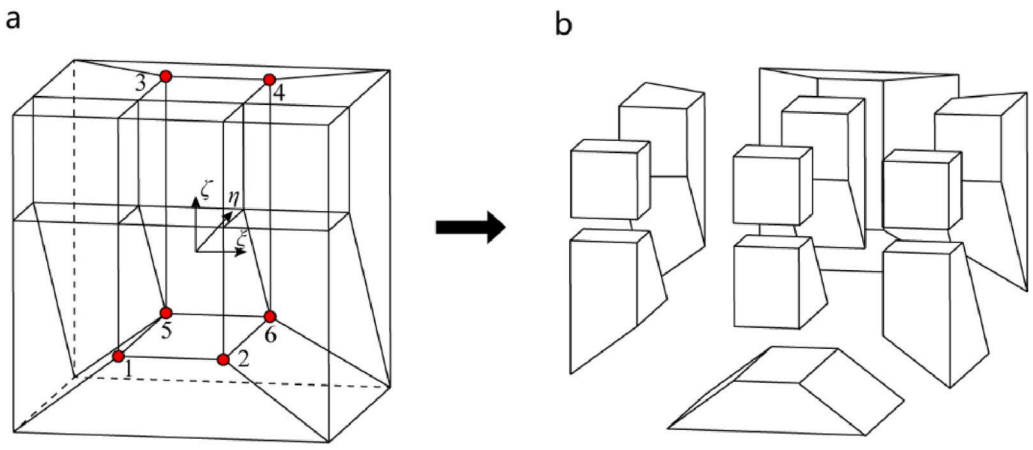

Fig. 7. Subdivision details of refinement template (b). (a) Inserted nodes 1 to 6 (colored in red); (b) Exploded view of the refined elements. (For interpretation of the references to color in this figure legend, the reader is referred to the Web version of this article.)

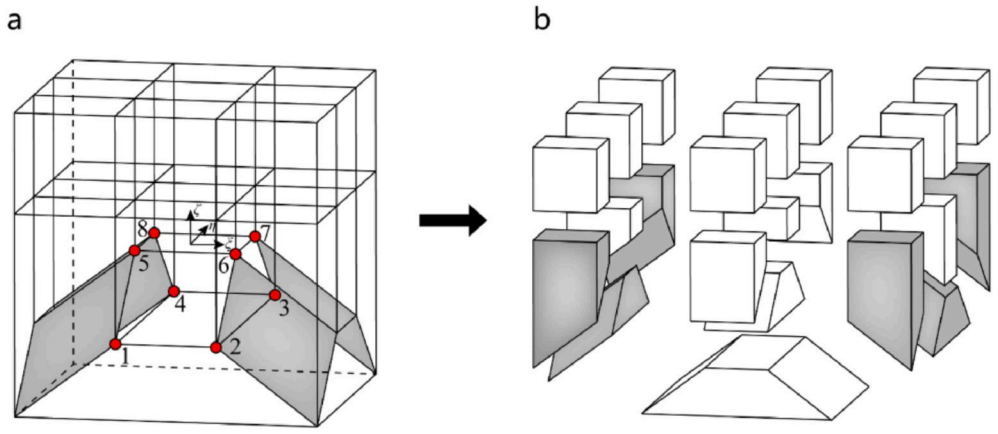

Fig. 8. Subdivision details of refinement template (c). (a) Inserted nodes 1 to 8 (colored in red) and related element faces (colored in grey); (b) Exploded view of the refined elements. (For interpretation of the references to color in this figure legend, the reader is referred to the Web version of this article.)

Table 1
Natural coordinates of inserted nodes of templates (b) and (c).

Inserted nodes		1	2	3	4	5	6	7	8
Template (b)	ξ	$-\frac{1}{3}$	$\frac{1}{3}$	$-\frac{1}{3}$	$\frac{1}{3}$	$-\frac{1}{3}$	$\frac{1}{3}$	/	/
	η	-1	-1	$\frac{1}{2}$	$\frac{1}{2}$	$\frac{1}{2}$	$\frac{1}{2}$		
	ζ	$-\frac{1}{2}$	$-\frac{1}{2}$	1	1	$-\frac{1}{2}$	$-\frac{1}{2}$		
Template (c)	ξ	$-\frac{1}{3}$	$\frac{1}{3}$	$\frac{1}{3}$	$-\frac{1}{3}$	$-\frac{1}{3}$	$\frac{1}{3}$	$\frac{1}{3}$	$-\frac{1}{3}$
	η	-1	-1	1	1	$-\frac{1}{3}$	$-\frac{1}{3}$	$\frac{1}{3}$	$\frac{1}{3}$
	ζ	$-\frac{1}{2}$	$-\frac{1}{2}$	$-\frac{1}{2}$	$-\frac{1}{2}$	0	0	0	0

mesh refinement, the known displacement field can be simply mapped to the newly added conventional nodes using the standard shape function.

3.2. Integration of enriched elements

Numerical integration of enriched elements without fragmentation points has been discussed in our previous work (Shi and Liu, 2021). The partitioning process of enriched elements with fragmentation points will be detailed in this section in the context of explicit crack surface representation. As shown in Fig. 9a, a portion of an explicit crack surface included in a tip-enriched element, is made up of six triangular patches, namely $P_s-P_1-P_2$, $P_s-P_2-I_1$, $P_s-I_1-P_3$, $P_s-P_3-P_4$, $P_3-I_2-P_4$, and $P_s-P_4-P_5$, where P_1 to P_5 are intersection points of fracture face and element faces, P_s denotes segmentation point, and I_1 to I_2 are intersection points of fracture face and element edges. Then, the partitioning can be performed according to the following steps:

(1) Get the angular bisector of $P_1-P_s-P_5$ and obtain its intersection point P_e with element face, then create the triangular patches $P_s-P_e-P_1$ and $P_s-P_5-P_e$, as illustrated by the green surfaces in Fig. 9b.
(2) Extend $P_s-P_e-P_1$ and $P_s-P_5-P_e$ to get intersection points I_3 to I_4, and then create triangular patches $I_3-P_1-P_e$ and $I_4-P_e-P_5$, as illustrated by the fuchsia surfaces in Fig. 9b.
(3) As shown in Fig. 9c and d, divide the initial element to the upper section and the lower section. As illustrated by the red lines, partition the surfaces of both sections into triangles according to the polygon triangulation scheme (Lo, 2015).
(4) Get the centroid of each section and then create tetrahedra by connecting triangular patches formed in step (3) and the centroid for each section.

3.3. Crack propagation criterion

Existing literature on 3D crack growth simulation using the XFEM commonly use the SIFs-based crack propagation criteria, for example,

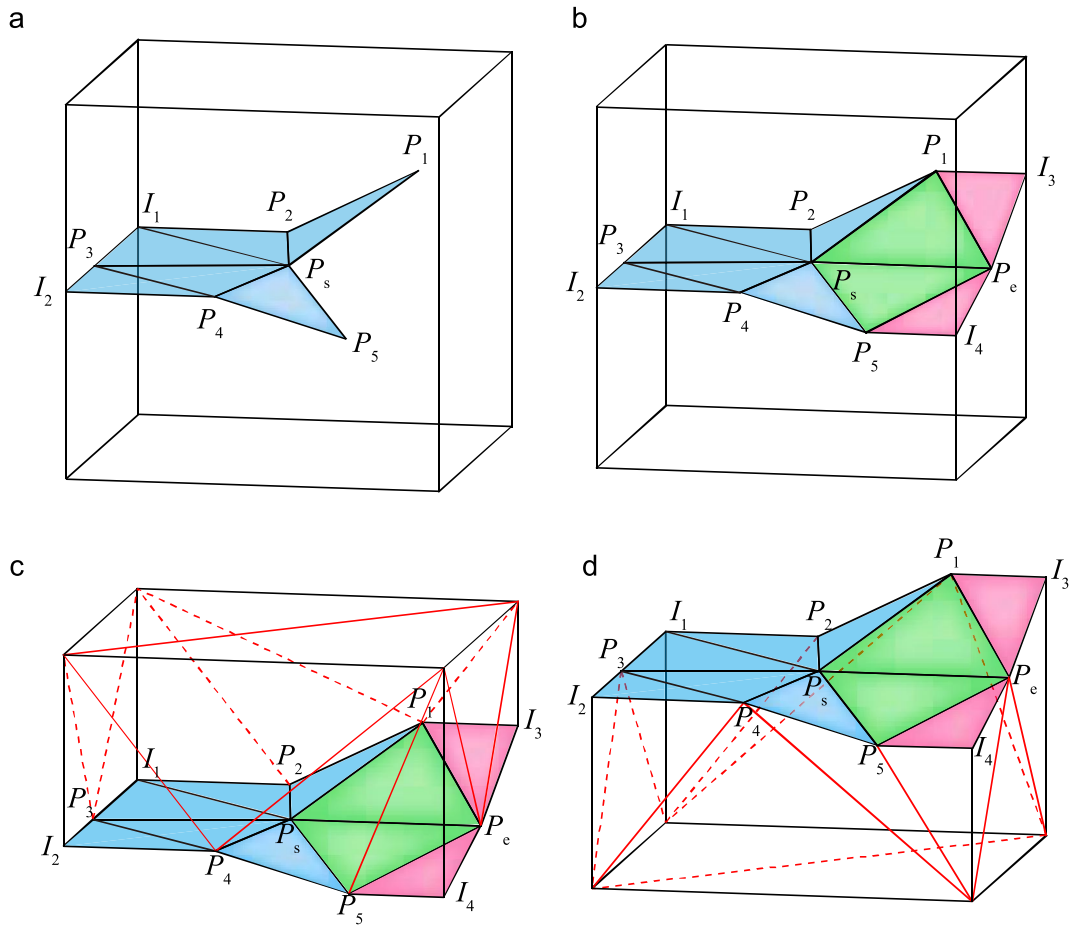

Fig. 9. Partitioning process of the tip-enriched element which includes a segmentation point to perform numerical integration. (a) The crack surface and the segmentation point in tip-enriched element. (b) Extension of the crack surface. (c) The upper section of the enriched element. (d) The lower section of the enriched element.

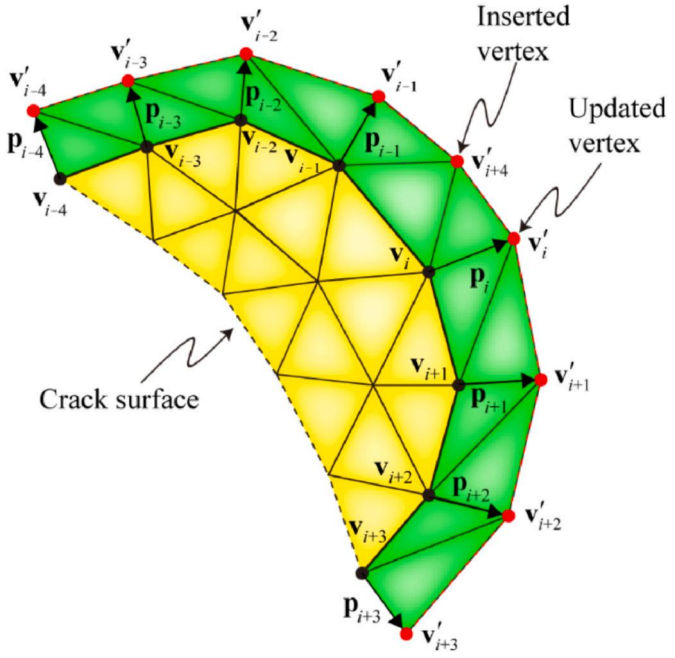

Fig. 10. Illustration of the crack front vertices updating process in the context of explicit crack surface description. $\mathbf{v}'_{i+4}$ is a vertex inserted at the midpoint of vertices $\mathbf{v}'_{i-1}$ and $\mathbf{v}'_{i}$.

the Schöllmann's criterion (Lazarus et al., 2008; Pereira et al., 2010; Shi and Liu, 2021; Wolff et al., 2020). However, owing to the complex geometrical features of 3D fractures, the excellent performance and high accuracy of SIFs computation in the 2D XFEM models may not be simply replicated in the 3D XFEM simulations (Tian et al., 2019; Xiao et al., 2021), especially when considering the crack front segmentation phenomenon (Doitrand and Leguillon, 2018). On the other hand, laboratory experiments and simulations based on the phase-filed method indicate that criteria based on the stress field are capable of modeling crack propagation in brittle materials under mixed loading conditions (Doitrand and Leguillon, 2018; Dumstorff and Meschke, 2007; Lin et al., 2010; Meng et al., 2013; Remij et al., 2015). As a typical representative, the maximum principal stress (MPS) criterion has been widely adopted in rock engineering including hydraulic fracturing simulations (Jamaloei, 2021; Lecampion et al., 2018; Liu et al., 2019; Rivas and Gracie, 2020). Therefore, in this study, the MPS criterion together with the local mesh refinement strategy is adopted instead of conventional SIFs-based criteria.

Since the stress distribution along the crack periphery is unknown, in this study, the weighted average stress tensor $\boldsymbol{\sigma}$ inside a sphere of radius r centered on the crack front vertex is computed by

$$\boldsymbol{\sigma} = \sum_{i=1}^{ng} \boldsymbol{\sigma}_i w_i \Big/ \sum_{i=1}^{ng} w_i \tag{26}$$

in which $\boldsymbol{\sigma}_i$ is the stress tensor corresponding to Gauss point i, ng is the number of Gauss points inside the sphere, and w_i represents the weight function related to the distance l_i between the Gauss point i and

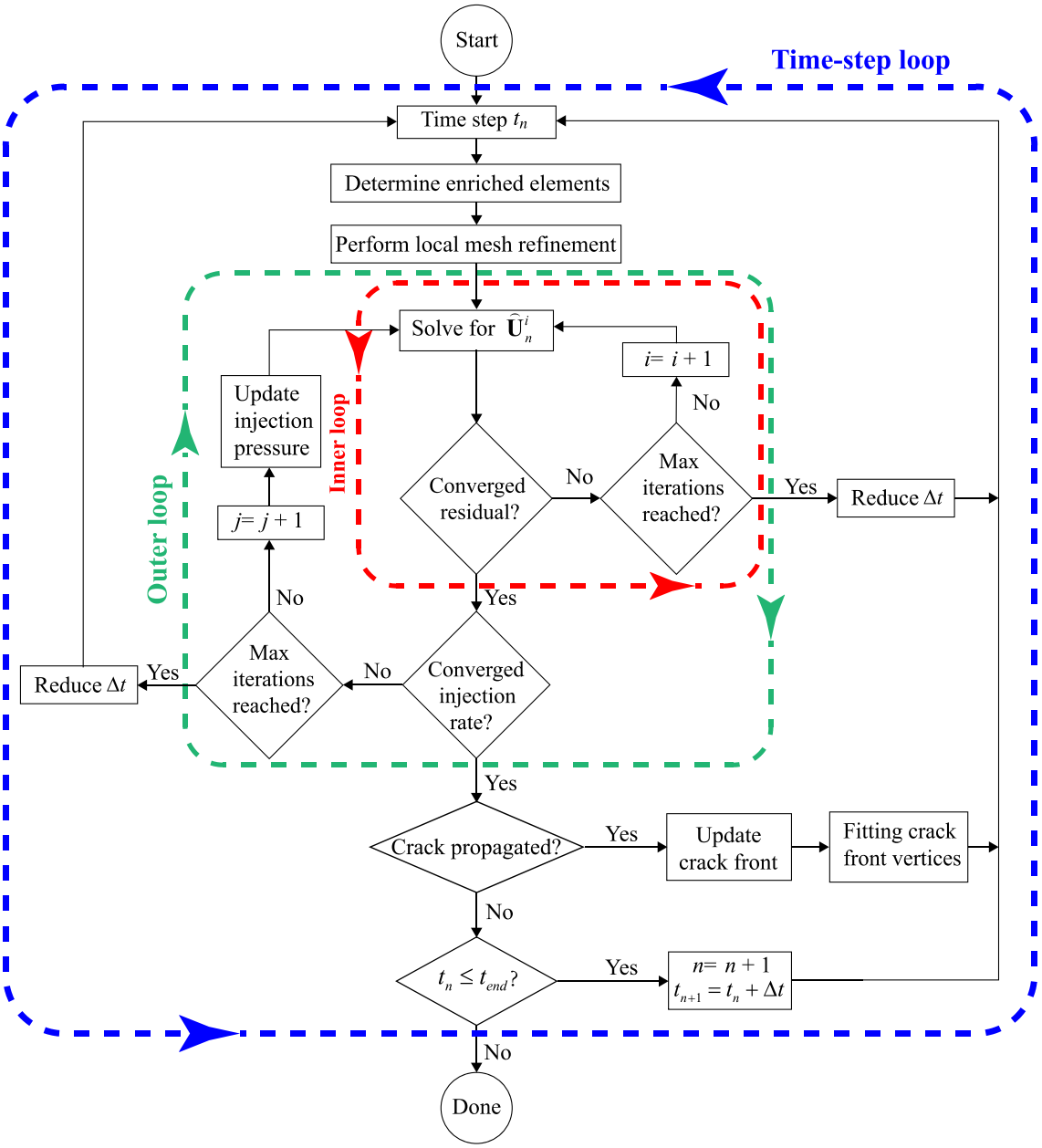

Fig. 11. Illustration of the program workflow which consists of three layers of loops: the time-step loop, the outer loop, and the inner loop. n, j, and i represent the time step index, the iteration step index of the outer loop, and the iteration step index of the inner loop, respectively. t_{end} is the desired ending time of the simulation.

the sphere center (Shi et al., 2022):

$$w_i = \left[1 - \left(\frac{l_i}{r}\right)^{\chi}\right]^3 \tag{27}$$

where χ is a control parameter that determines the rate of descent of w_i with the increase of l_i, and is taken as 5 (Shi et al., 2022) in this study. The sphere radius r is taken as the average size of all enriched elements.

The maximum principal stress σ_1^i of vertex i can be obtained after getting the weighted average stress tensor $\boldsymbol{\sigma}$. Then, as shown in Fig. 10, if σ_1^i exceeds the strength of rock formation s_t, the vertex $\mathbf{v}_i$ propagates to $\mathbf{v}_i'$ according to $\mathbf{v}_i' = \mathbf{v}_i + \mathbf{p}_i$ where:

$$\mathbf{p}_i = \Delta a_{\max} \frac{\sigma_1^i}{\bar{\sigma}_1} \mathbf{n}_r^i \tag{28}$$

in which $\Delta a_{\max}$ is a parameter that controls the propagation size, $\mathbf{n}_r^i$ is a vector perpendicular to the direction of σ_1^i and located in the normal plane of the smoothed crack front f (as will be shown in Section 3.4) at $\mathbf{v}_i$, and $\bar{\sigma}_1$ denotes the average value of principal stress along the curve f:

$$\bar{\sigma}_1 = \frac{\oint \sigma_1 df}{\oint df} \tag{29}$$

It's worth noting that if the distance between two consecutive vertices, for example, $\mathbf{v}_{i-1}'$ and $\mathbf{v}_i'$ is greater than $1.5l_c$, an additional vertex needs to be inserted at $(\mathbf{v}_{i-1}' + \mathbf{v}_i')/2$, just as illustrated in Fig. 10.

3.4. Fitting of crack front vertices

Once the propagated crack front is available, considering the complexity of the crack front fragmentation, it is certainly preferable to increase its geometric smoothness and thus to acquire a more robust result. To this end, the cubic smoothing spline technique (Boor, 2001) is

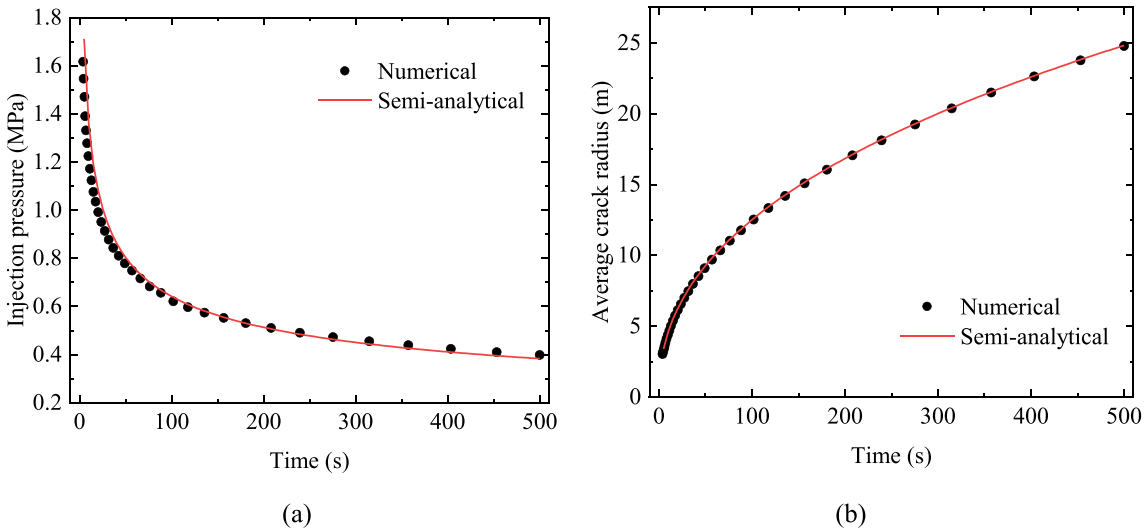

Fig. 12. Variations of average crack radius (a) and injection pressure (b) over time. The semi-analytical results (Dontsov, 2016) are also shown.

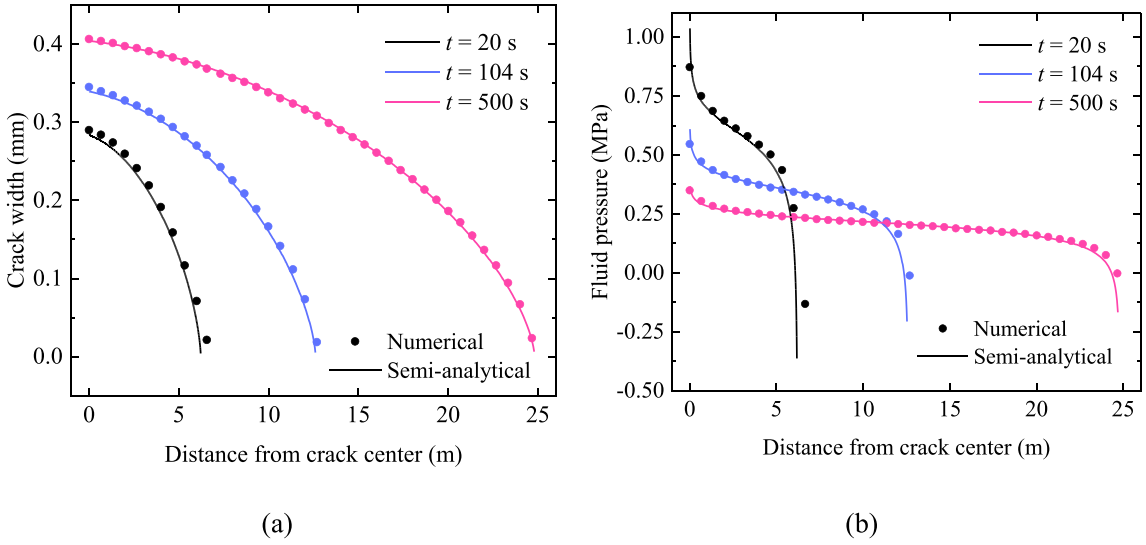

Fig. 13. Profiles of average crack width (a) and fluid pressure (b) along the radius at time instants 20 s, 104 s, and 500 s. The semi-analytical results (Dontsov, 2016) are also shown.

adopted to adjust the locations of crack front vertices. For a collection of successive crack front vertices $\mathbf{v}_i'$ $(i=1,\quad 2,\cdots,\quad n)$ starting from and ending at fragmentation points, the smoothed vertices can be obtained by finding the cubic spline f which minimizes the following expression (Boor, 2001):

$$p\sum_{i=1}^{n}\widehat{w}_i\left|\mathbf{v}_i'-f(s)\right|^2+(1-p)\int\left|D^2f(s)\right|^2ds \tag{30}$$

in which the first term is used for error measure and parameters p, $\widehat{w}_i$, s are the smoothing factor, the error measure weights, and the curvilinear coordinate system of spline f, respectively. In this paper, p and $\widehat{w}_i$ are taken as 0.95 and 1, respectively. In the above expression, the second term is used for roughness measure and D^2f is the second derivative of cubic spline f.

3.5. Program workflow

The fully coupled fluid-solid numerical model based on the XFEM has been coded into an in-house code named as PhiPsi (http://phipsi.top).

The program workflow is illustrated in Fig. 11. Within each time step (see the blue dashed box in Fig. 11 for the time-step loop), there exist two loops: the inner loop indexed by i (the red dashed box in Fig. 11) which solves the fluid-solid coupling equations using the N-R method, and the outer loop indexed by j (the green dashed box in Fig. 11) which adjusts the injection pressure P_{inj} to fulfill the global mass conservation law according to the following equation (Khoei et al., 2015; Rivas and Gracie, 2020):

$$P_{inj}^{j+1}=P_{inj}^{j}+\lambda^j\left(\frac{1}{\Delta t}\sum_e\Delta w_eA_e+\sum_eQ_L^eA_e-Q_{inj}\right) \tag{31}$$

where Δw_e is the change of the crack width of fluid element e, A_e represents fluid element area, and $\lambda=\partial P_{inj}/\partial Q$. The time-step size Δt is adaptively reduced by 50% if either the inner loop or outer loop fails to convergence after reaching the maximum number of iterations.

4. Verification

In this section, four examples are presented to show the capability

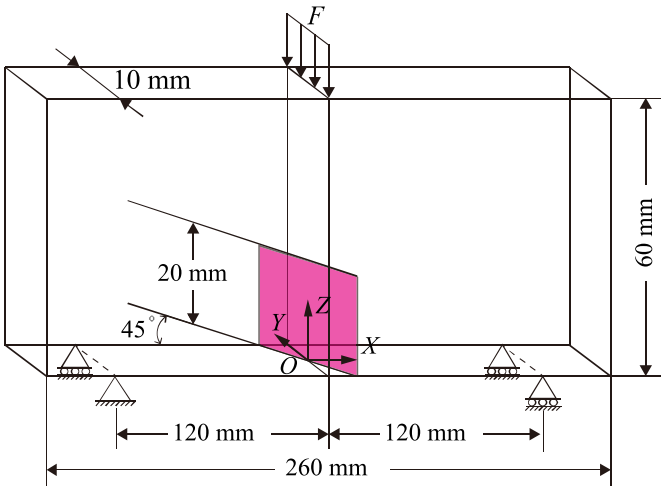

Fig. 14. Illustration of an initial crack (colored in fuchsia) inside a beam under the three-point bending test condition.

and reliability of the suggested numerical model. The first one is to illustrate the computational accuracy of hydraulic fracturing simulation by comparison with the semi-analytical solution that accounts for fluid leak-off (Dontsov, 2016). The second one is aim to show the ability of modeling crack propagation under mixed loading condition by comparison with experimental results. Besides, the third example focuses on the simulation capability of the crack front segmentation process and investigates the effects of segmentation on crack paths. Finally, the last example simulates the crack front segmentation during the hydraulic fracturing process of a radial crack in the cylindrical PMMA specimen under the combined I-III loading conditions.

4.1. Fluid-driven penny-shaped crack

The evolution of a penny-shaped crack with an initial radius of 3 m which is centrally and horizontally embedded inside a block medium of size 150 × 150 × 50 m (in x, y, and z directions, respectively) is simulated in this example. The medium has an elastic modulus E of 30 GPa, a Poisson's ratio ν of 0.35, a fracture toughness K_{Ic} of 0.5 MPa·m$^{1/2}$, and a leak-off coefficient C_L of $0.5 \times 10^{-6}\mathrm{m}/\sqrt{s}$. The fluid has a viscosity of 0.001 Pa·s and is injected through the crack center at a constant rate of 0.01 m^3/s. All faces of the block are subjected to roller boundary conditions. A cubic zone of size 60 × 60 × 3 m (in x, y, and z directions, respectively) around the crack is meshed with elements of size 0.5 × 0.5 × 0.5 m and the resulting total number of elements is 304,704. In this example, however, the SIFs-based maximum circumferential stress criterion (Baydoun and Fries, 2012), instead of the proposed MPS criterion, is employed as the propagation criterion to perform a comparison with analytical solutions. Besides, the local mesh refinement has not been used in this example since the crack is in a simple mode-I situation. The simulation ends when the pumping time exceeds 500 s.

The evolutions of injection pressure and average crack radius with time are presented in Fig. 12, in which the semi-analytical solutions

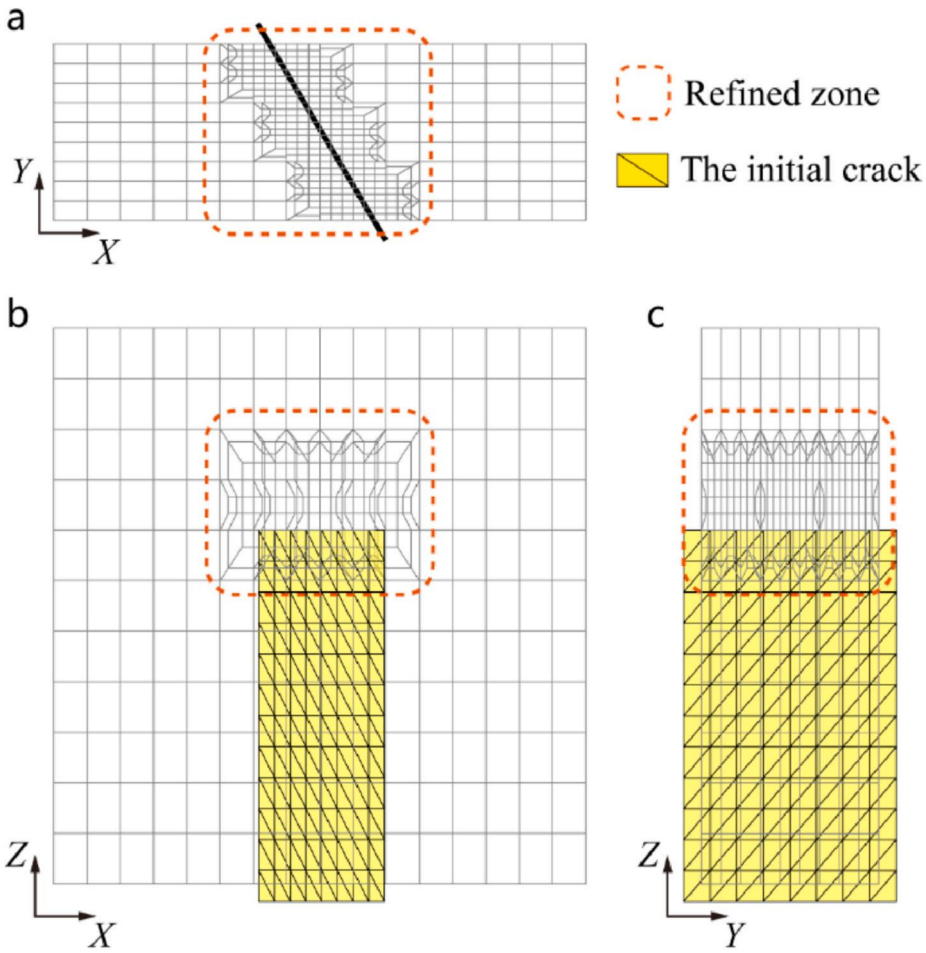

Fig. 15. Zoom views of finite element mesh after performing local mesh refinement of tip-enriched elements for the initial crack: (a) the *XY*-plane view, (b) the *XZ*-plane view, and (c) the *YZ*-plane view. The initial crack is discretized with triangular patches colored in yellow. (For interpretation of the references to color in this figure legend, the reader is referred to the Web version of this article.)

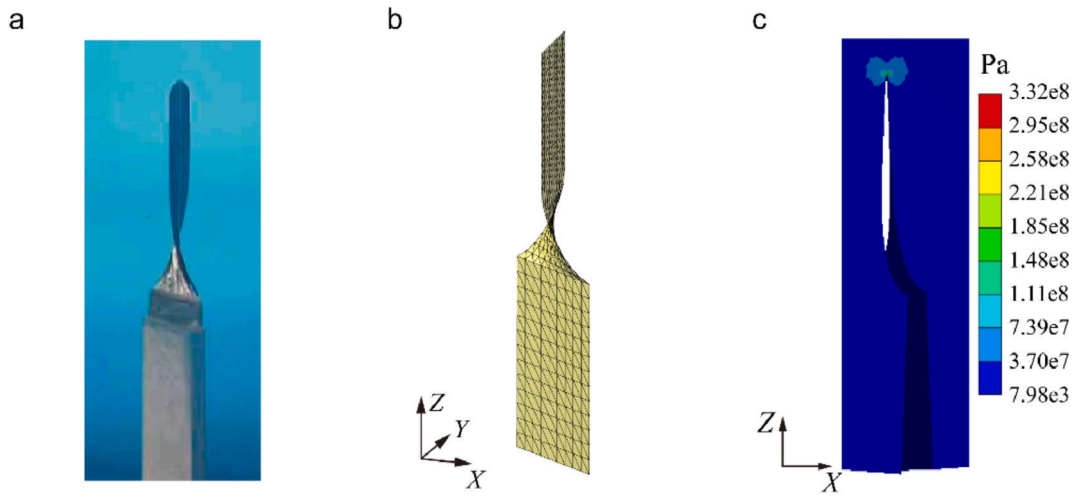

Fig. 16. Crack propagation paths of the three-point bending experiment: (a) the experimentally obtained path (Lazarus et al., 2008), (b) the numerically obtained path, and (c) the von-Mises stress contour around the crack tip.

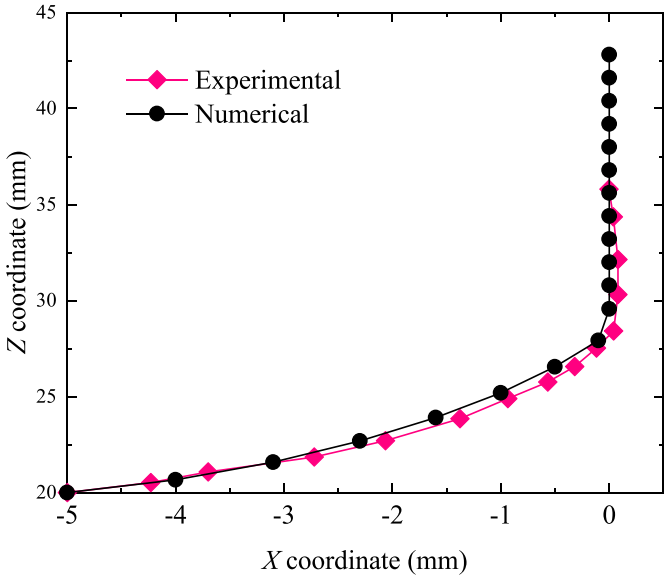

Fig. 17. Comparison of crack tip positions in the rear face ($Y = 5$ mm) of the model.

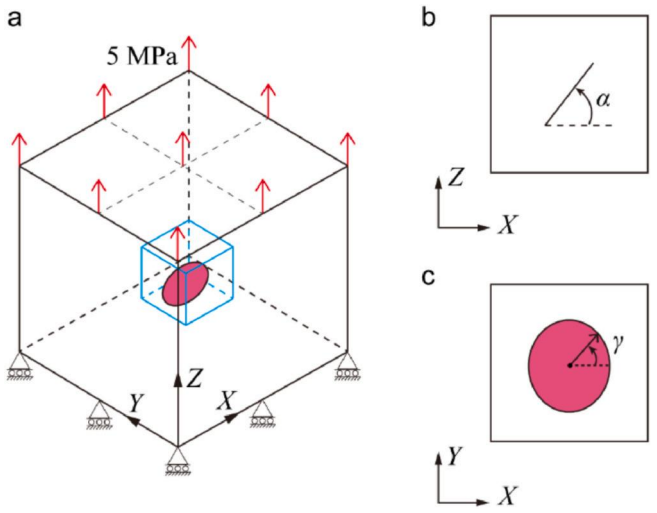

Fig. 18. Depiction of a penny-shaped crack (colored in fuchsia) in a linear-elastic block model. (a) Boundary conditions and external stress; (b) incline angle α; and (c) angle γ to mark the crack tip position. In figure (a), the zone marked with blue lines surrounding the initial crack is meshed with finer elements. (For interpretation of the references to color in this figure legend, the reader is referred to the Web version of this article.)

(Dontsov, 2016) that account for the roles of fluid viscosity, fracture toughness, as well as fluid leak-off are also shown. Detailed Matlab codes for the semi-analytical solutions can be found on GitHub (https://github.com/PhiPsi-Software/PC_analytical_solution). In addition, the average crack width and fluid pressure distributions along the radius at time instants 20 s, 104 s, and 500 s are given in Fig. 13. It is shown that the numerical results are quantitatively consistent with the analytical ones in both figures, indicating the reliability of the proposed numerical model to perform hydraulic fracturing simulations.

4.2. Three-point bending experiment

In this section, a three-point bending experiment performed by Lazarus et al. (Lazarus et al., 2008; Citarella and Buchholz, 2008) is simulated to replicate the evolution of a skew crack placed at the bottom of a beam specimen made of PMMA. The model geometry, boundary conditions, and the external force F are shown in Fig. 14 in which the initial crack is under mixed-mode I/II/III loading (Lazarus et al., 2008). The parameters are taken as $E = 2.8$ GPa, $\nu = 0.3$, $s_t = 15$ MPa (Lazarus et al., 2008; Wolff et al., 2020), and $\Delta a_{\max} = 1.2$ mm. The model is meshed with 11,088 elements in total. Zoom views of the mesh after performing local mesh refinement of tip-enriched elements for the initial crack are presented in Fig. 15. It needs to be mentioned that in this example the primary goal is to evaluate the capacity of the established model to cope with mixed-mode fracture propagation and hence the splitting of the crack front has not been considered here.

The crack propagation path captured experimentally by Lazarus et al. (Citarella and Buchholz, 2008; Lazarus et al., 2008), the crack geometry obtained numerically in this study, and the calculated von-Mises stress distribution surrounding the crack front are shown in Fig. 16. From Fig. 16b and c, it can be concluded that the crack sharply twists and then grows almost planarly in a predominantly mode-I situation, which is in accordance with the experimentally recorded crack path shown in Fig. 16a. A comparison of crack tip positions in the rear face ($Y = 5$ mm) of the model is presented in Fig. 17, through which a quantitative evaluation of the simulation accuracy is available. It can be found that the simulated crack path coincides well with the

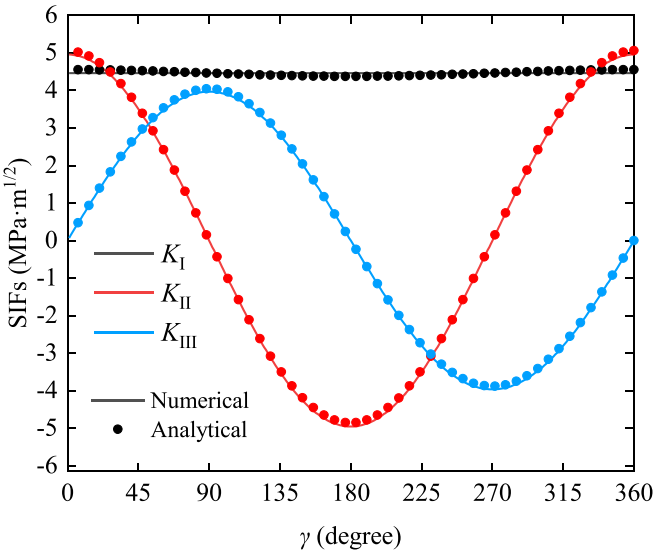

Fig. 19. Distributions of the numerical and analytical SIFs along the initial crack front.

experimental one, confirming the capability of the proposed numerical strategy to predict crack propagation under mixed loading conditions.

4.3. Effects of segmentation on crack paths

In this example, the crack front segmentation process in mode I-II-III is reproduced during the propagation of a penny-shaped crack inside a cube of size 50 × 50 × 30 m (in x, y, and z directions, respectively). As depicted in Fig. 18a, the bottom of the cube is fixed and the top face is undergoing an external stress of 5 MPa. The incline angle α of the initial crack of radius $a = 2.5$ m is 45°. The angle γ is introduced to mark the position of the crack front, as shown in Fig. 18c. Parameters E, ν, s_b, and Δa_{max} are respectively set to 20 GPa, 0.2, 5 MPa, and 0.25 m. A zone of size 9 × 9 × 5 m (in x, y, and z directions, respectively) around the initial crack is meshed with finer elements of size 0.3 × 0.3 × 0.3 m and the total number of elements is 25,725. The crack stops propagating after eight steps and then the resulting crack geometries for the cases with and without incorporating the crack front fragmentation process will be

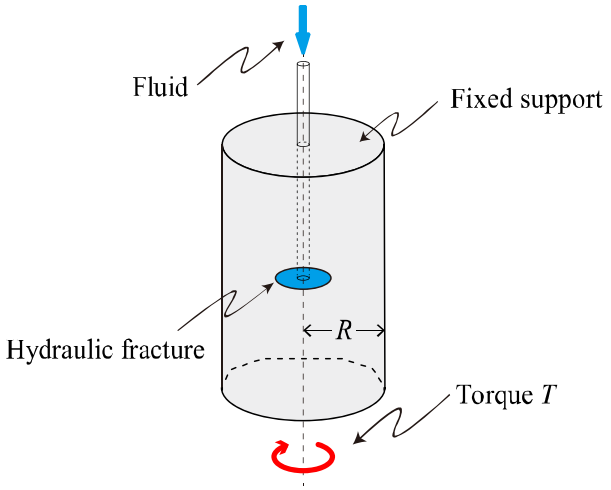

Fig. 21. Schematic plot of the laboratory-scale experiments performed by Wu et al. (2009). The top surface of the cylinder is fixed.

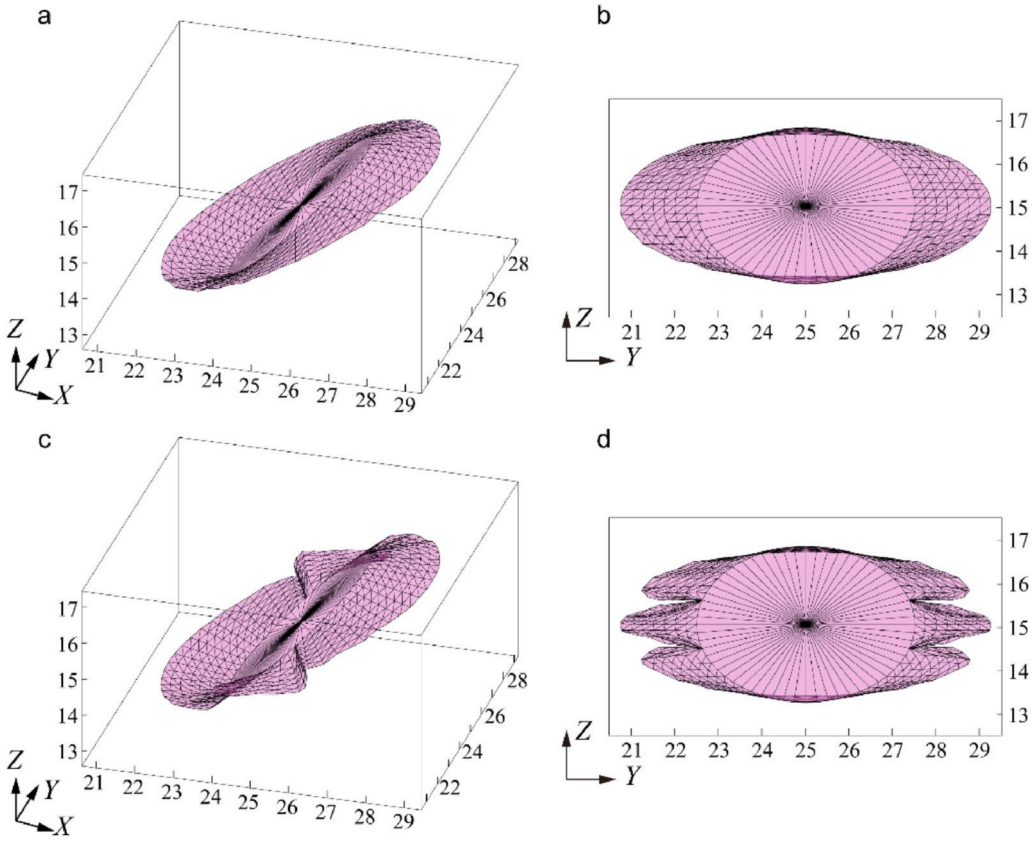

Fig. 20. Comparison of crack geometries after eight growth steps without (figures (a) and (b)) and with (figures (c) and (d)) fragmentation of crack front. The coordinates are in meters.

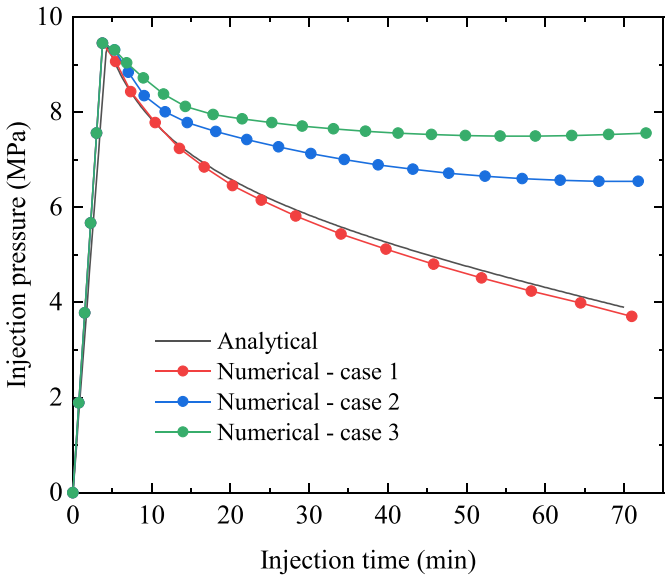

Fig. 22. Evolutions of fluid pressure over time of cases 1 to 3. The analytical solution without segmentation is also shown.

compared.

The analytical SIFs along the front of a penny-shaped crack is available as follows (Duflot, 2006):

$$\begin{cases} K_{\mathrm{I}} = 2\sigma\cos^2\alpha\sqrt{\dfrac{a}{\pi}} \\ K_{\mathrm{II}} = -\dfrac{4}{2-\nu}\sigma\sin\alpha\cos\alpha\sqrt{\dfrac{a}{\pi}}\sin\gamma \\ K_{\mathrm{III}} = -\dfrac{4(1-\nu)}{2-\nu}\sigma\sin\alpha\cos\alpha\sqrt{\dfrac{a}{\pi}}\cos\gamma \end{cases} \tag{32}$$

which has been plotted in Fig. 19. It can be noticed that the splitting of crack front might be triggered near the crack periphery in mixed-mode I-III where $\gamma = \pi/2$ and $3\pi/2$. In this example, four fragmentation points are selected at $\gamma = 2\pi/5$, $3\pi/5$, $7\pi/5$, and $8\pi/5$. The comparison of crack geometries is given in Fig. 20, from which the influence of crack front fragmentation can be noticed. In contrast to the crack morphology exhibited in Fig. 20a and b, the segment in the mixed-mode I-III section tends to rotate towards the mode-I direction, resulting in a more complicated crack morphology, as shown in Fig. 20c and d. Besides, it can be seen that the final crack paths in the mixed-mode I-II zone (where $\gamma = 0$ and π) in both scenarios are nearly identical, confirming that segmentation influences only mixed-mode I-III crack front.

4.4. Comparison with hydraulic fracturing experiment

In this example, the laboratory-scale hydraulic fracturing experiments performed by Wu et al. (2009) will be simulated to investigate the influence of crack front segmentation. As depicted in Fig. 21, an initial crack of radius $a = 1.25$ cm is centrally placed in a PMMA cylinder of radius $R = 5$ cm and height $H = 20$ cm. The fluid is pumped through a metal pipe along the axis of the cylinder. By applying the torque $T = 500$ N·m, the initial hydraulic fracture is under mode I + III condition with a constant $K_{\mathrm{III}}/K_{\mathrm{I}}$ ratio along the crack periphery. Parameters E, ν, s_t, K_{Ic}, and $\Delta a_{\max}$ are set to 3.32 GPa, 0.38, 40 MPa, 1.21 MPa·m$^{1/2}$, and 0.2 cm, respectively (Mark, 2009; Wu et al., 2009). In addition, fracturing parameters including fluid pumping rate Q_{inj}, fluid viscosity μ, and fracturing time are set to 0.006 mL/min, 0.01 Pa·s, and 70 min, respectively (Wu et al., 2009).

According to the semi-analytical solution (Dontsov, 2016) of fluid-driven penny-shaped crack, it can be seen that the fracturing is toughness-dominated and thus constant pressure distribution can be assumed within the crack. Then, in light of the analytical solutions (Tada et al., 2000) of crack under uniform pressure in the cylinder, the variations of crack radius r_c and fluid pressure P can be written as:

$$r_c(t) = \begin{cases} a\,, & if \quad t \le t_s \\ \left(\dfrac{3Q_{inj}Et}{8\sqrt{\pi}(1-\nu^2)K_{\mathrm{Ic}}}\right)^{2/5}, & if \quad t > t_s \end{cases} \tag{33}$$

$$P(t) = \begin{cases} \dfrac{3Q_{inj}Et}{16a^3(1-\nu^2)G(a/R)}\,, & if \quad t \le t_s \\ \dfrac{\sqrt{\pi}K_{\mathrm{Ic}}}{2\sqrt{r_c}F(r_c/R)}\,, & if \quad t > t_s \end{cases} \tag{34}$$

in which G and F are functions related to geometric parameters (Tada et al., 2000), and t_s denotes the time instant of propagation occurs:

$$t_s = \frac{8\sqrt{\pi}(1-\nu^2)K_{\mathrm{Ic}}a^{5/2}}{3EQ_{inj}} \tag{35}$$

Besides, the $K_{\mathrm{III}}/K_{\mathrm{I}}$ ratio has the form

$$\frac{K_{\mathrm{III}}}{K_{\mathrm{I}}} = \frac{4Ta}{3\pi P(t)R^4} \tag{36}$$

Submitting parameters into Eq. (35) yields $t_s = 4.29$ min, then $P(t_s)$ can be determined according to Eq. (34) as 9.45 MPa. Finally, the result of $K_{\mathrm{III}}/K_{\mathrm{I}}$ at time instant t_s can be computed as 4.49%.

Cases with no segment (case 1), 5 segments (case 2), and 7 segments (case 3) are comparatively simulated using a mesh with 27,040 elements to investigate the influence of the splitting of crack front. In case 1, the torque T has been ignored in order to reach a mode-I condition and

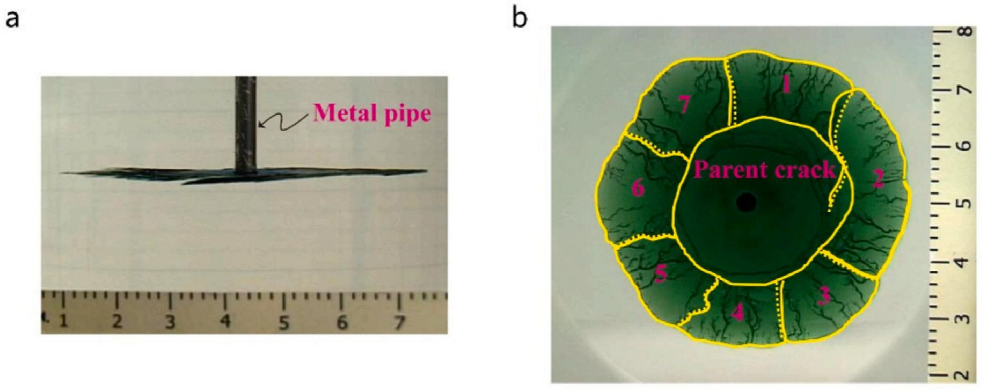

Fig. 23. Hydraulic fracture recorded in experiments carried out by Wu et al. (2009): (a) the front view and (b) the bottom view of the crack with 7 segments. In the right figure, overlapped sections between neighboring segments can be seen (for example, between segments 1, 2 and segments 3, 4).

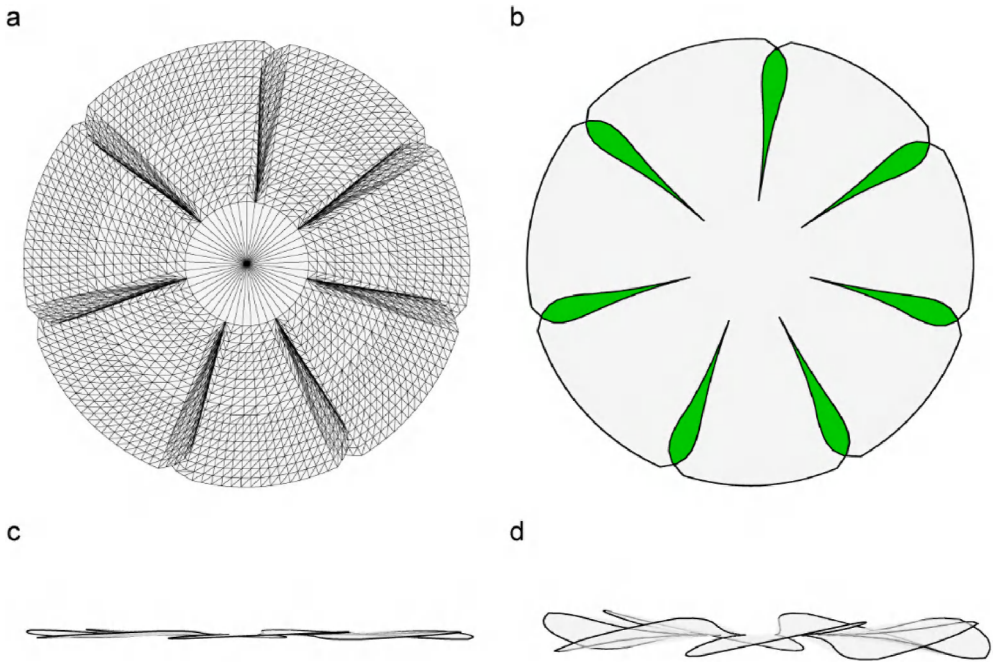

Fig. 24. Illustration of the numerically obtained hydraulic fracture with 7 segments: (a) bottom view, (b) bottom view with overlapped region highlighted (colored in green), (c) front view, and (d) front view with a scaling factor of 20. (For interpretation of the references to color in this figure legend, the reader is referred to the Web version of this article.)

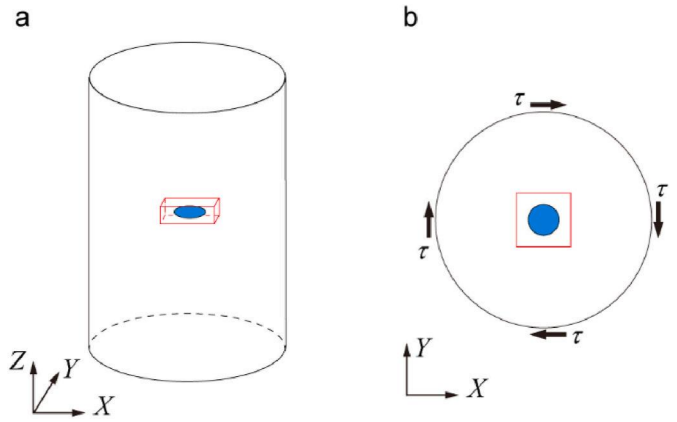

Fig. 25. Depiction of a penny-shaped fluid-driven crack (colored in blue) in a linear-elastic cylindrical model. (a) the general view, and (b) the vertical view. The refined zone is marked with red lines. (For interpretation of the references to color in this figure legend, the reader is referred to the Web version of this article.)

compare with the analytical solution. Crack segments are evenly distributed along the crack periphery in cases 2 and 3. Fig. 22 depicts the evolutions of injection pressure over time. It can be observed that the curve of case 1 agrees well with the analytical one. Furthermore, as the segment number grows from zero to 5, and then subsequently to 7, the injection pressure rises considerably. In particular, the resultant injection pressure rises 76.5 percent from 3.71 MPa in case 1 to a much higher value of 6.55 MPa in case 2, and then rises another 15.4 percent to 7.56 MPa in case 3 in comparison with case 2. This anomalous phenomenon of pressure build-up found in the simulation is consistent with Wu's experimental findings (Wu et al., 2009).

In Fig. 23, the hydraulic fracture with 7 segments obtained by Wu et al. (2009) is shown. By comprising with the simulated results shown in Fig. 24, it can be noticed that in both figures there exist overlapping sections between neighboring segments, and segments are inclined at minor angles to their initial parent cracks. It has been widely known that during hydraulic fracturing the stress shadowing effects between adjacent fractures have a major impact on fracture propagation (Shi et al., 2016). As a result, it's possible that the interactions between overlapped segments are the main causes of the fluid pressure build-up observed in Fig. 22. On the other hand, the unbroken parts between neighboring segments hinder the crack from further opening, hence causing the rise of required pressure. Accordingly, it can be argued that disregarding crack segmentation for a hydraulic fracturing simulation in mixed-mode I + III situation might grossly underestimate the fluid pressure, thus resulting in potentially unreliable numerical solutions.

5. Results and discussion

Field data (Economides and Martin, 2007), laboratory experiments (Abass et al., 1996; Wu et al., 2009), as well as simulations (Fu and Bunger, 2019; Huang et al., 2013) have shown that hydraulic fractures are usually under mixed loading conditions induced by the combined effects of stress shadowing, existence of geological discontinuities, misalignment of perforations, inhomogeneous distribution of in-situ stress, and heterogeneous rock medium. In this section, the relations between the crack front segmentation and some key parameters will be studied systematically. In this paper, as shown in Fig. 25, a cylinder (of radius 40 m and height 120 m) is adopted to perform the simulation since the uniform distribution of shear stress along the crack front cannot be easily obtained using the widely adopted cubic model. The model parameters are chosen according to typical hydraulic fracturing treatments in shale gas formation (Ahrens, 1995; Economides and Martin, 2007; Haddad and Sepehrnoori, 2016). The radius of the initial crack which is horizontally located at the model center is 3 m. The radial confining pressure and the axial pressure are all taken as 10 MPa. As depicted in Fig. 25, the external shear force $\tau = 2$ MPa is applied to the sides of the cylinder to obtain a mixed-mode I/III condition. The refined block of size $25 \times 25 \times 5$ m (marked with red lines) is discretized with elements of size $0.4 \times 0.4 \times 0.4$ m and the resulting total number of elements is 90,738. Material parameters of the base case are taken as $E = 20$ GPa, $\nu = 0.25$, and $s_t = 5$ MPa. The length of the maximum

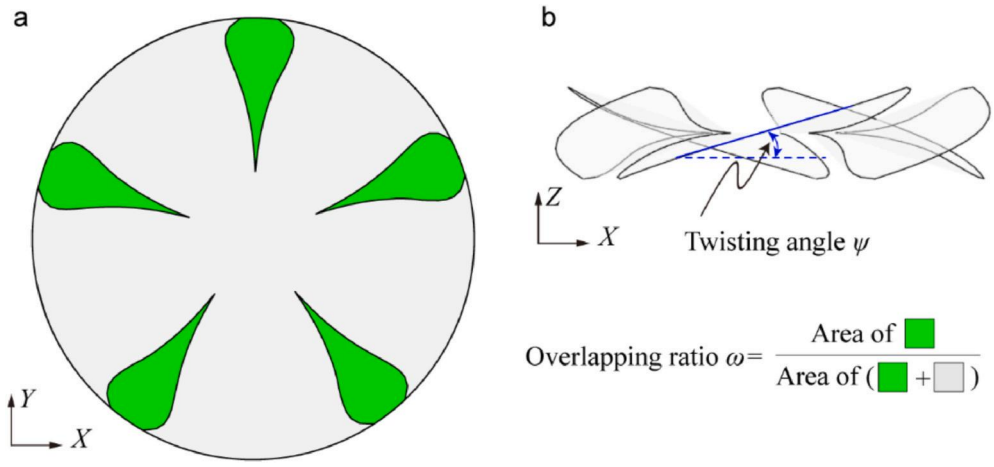

Fig. 26. Illustration of the numerically obtained hydraulic fracture with 5 segments: (a) top view with overlapped region highlighted in green, and (b) front view with a scaling factor of 10. The twisting angle ψ and the overlapping ratio ω are shown in the right figure. (For interpretation of the references to color in this figure legend, the reader is referred to the Web version of this article.)

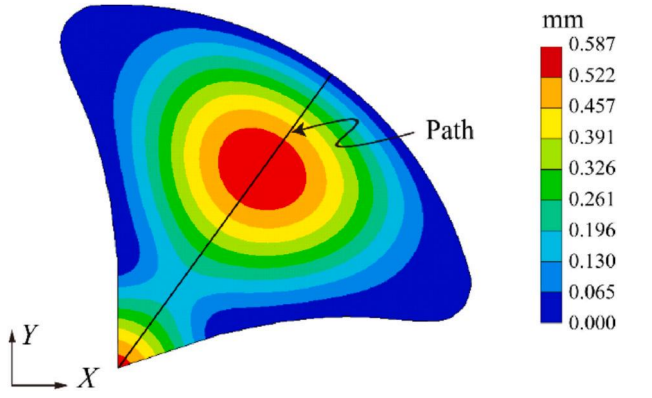

Fig. 27. Top view of the contour of crack aperture of the base case with crack front segmentation. Only one segment is shown due to the centrosymmetry of the model. A path is defined in this figure to plot the curve of crack aperture.

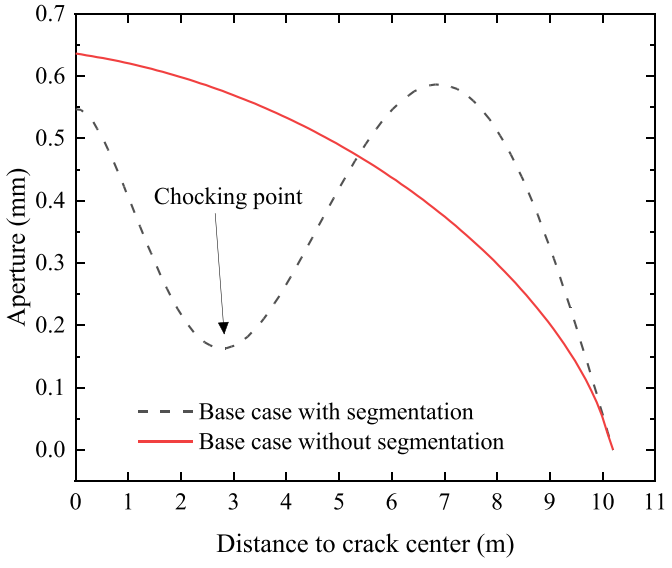

Fig. 28. Curves of crack aperture of the base case with and without crack segmentation along the path defined in Fig. 27.

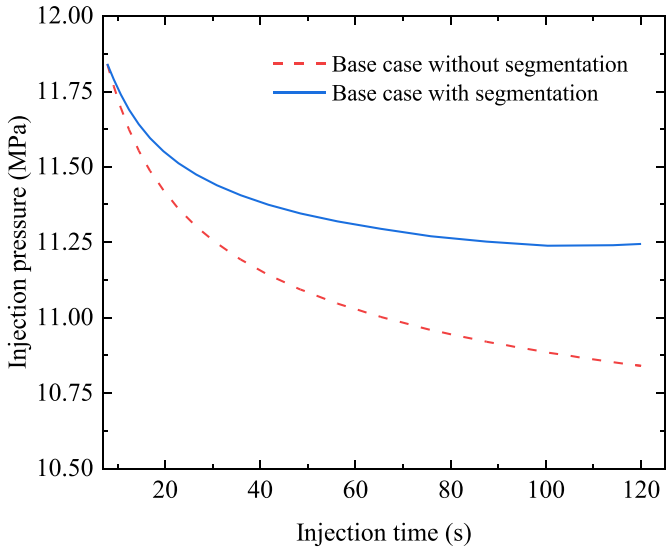

Fig. 29. Evolutions of fluid pressure over time of the base case with and without considering segmentation.

propagation step $\Delta a_{max}$is taken as 0.2 m. Fracturing parameters including fluid pumping rate Q_{inj}, fluid viscosity μ, Carter's leak-off coefficient C_L, and fracturing time are set to 0.001 m^3/s, 0.01 Pa·s, $0.5 \times 10^{-6} m/\sqrt{s}$, and 120 s, respectively. The number of segments is pre-specified as 5. It should be noted that before performing the hydraulic fracturing simulation, a static structural analysis is first run to ensure the initial equilibrium of geostress.

The propagation path in both top view and front view with a scaling factor of 10 is presented in Fig. 26 where the overlapped sections between segments are colored in green. The average radius of the final crack is 10.2 m. As shown in Fig. 26b, we define the twisting angle ψ to represent the degrees of segmentation. Since the positions and orientations of crack front segments are numerically available, ψ can be simply obtained and equals 1.7° in the base case. Besides, the overlapping ratio ω is defined as the ratio of overlapping area to the projected area of the entire crack surface in the *XY*-plane. The overlapping ratio ω can be accurately obtained using the wand tool in combination with the measure tool provided in the software ImageJ (Pascau and Pérez, 2013), and the value of ω in the base case is obtained as 16.95%. Contour of crack aperture of the base case with crack front segmentation is given in

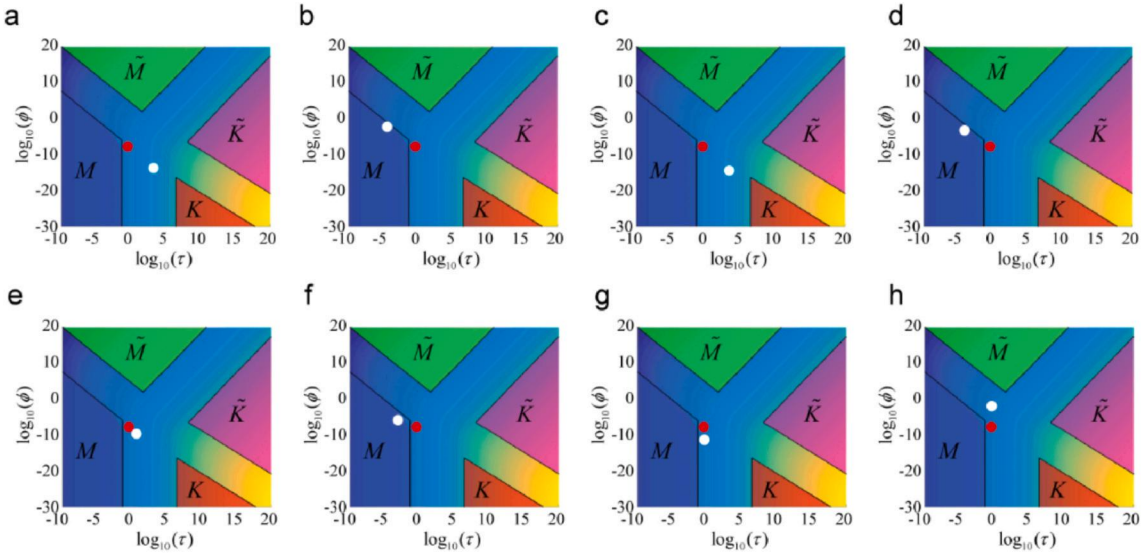

Fig. 30. Parametric maps of the propagation regime for the cases with (a) $E = 5$ GPa; (b) $E = 50$ GPa; (c) $\mu = 0.001$ Pa·s; (d) $\mu = 0.1$ Pa·s; (e) $Q_{inj} = 0.0005$ m^3/s; (f) $Q_{inj} = 0.005$ m^3/s; (g) $C_L = 0.5 \times 10^{-7}$ m/s$^{1/2}$, and (h) $C_L = 0.5 \times 10^{-5}$ m/s$^{1/2}$. The dimensionless parameters τ and ϕ (Dontsov, 2016) are taken as the average value of all vertices along the crack front of the initial crack. The red dots represent the base case and the white dots represent the sensitivity analysis cases. (For interpretation of the references to color in this figure legend, the reader is referred to the Web version of this article.)

Fig. 27. The distinct curves of crack apertures with and without crack segmentation along the path defined in Fig. 27 are presented in Fig. 28, where a choking point that might hinder the transport of proppant can be found. Evolutions of injection pressures over time of the base case with and without segmentation are shown in Fig. 29, from which the increase of fluid pressure can be noticed, just as mentioned in Section 4.4. Specifically, the increasing ratio χ of the final net pressure (i.e., injection pressure minus the in-situ stress σ_z) is 48.13%. It can also be seen that for the case without segmentation, the injection pressure continues to decrease. However, in the case with segmentation, the injection pressure tends to be flat and even has a tendency of increasing due to the interaction between overlapped segments shown in Fig. 26a.

5.1. Effects of elastic modulus

In this section, two different elastic moduli (a smaller one $E = 5$ GPa and a larger one $E = 50$ GPa) are considered while keeping other parameters unchanged. In order to compare the twisting angle ψ, all simulations continue until the crack radius reaches 10.2 m as obtained in the base case (similarly hereinafter). As shown in Fig. 30a and b, the parametric maps defined by dimensionless time parameter τ and leak-off parameter ϕ (Dontsov, 2016) are presented to show the position of the propagation regime of the initial crack front. Regions marked with M, K, $\tilde{M}$, and $\tilde{K}$ denote four limiting regimes of propagation (or vertex solutions), namely, storage viscosity, storage toughness, leak-off viscosity, and leak-off toughness, respectively (Dontsov, 2016). It can be seen that with the increases of E, the propagation regime shows a changing tendency from toughness dominated to viscosity dominated. The variations of injection pressure are given in Fig. 31a. To be specific, the increasing ratios χ of final net pressure for cases $E = 5$ GPa and $E = 50$ GPa are 65.94% and 32.82%, respectively. It can be found that χ decreases with the increase of elastic modulus E. The curve of crack aperture along the path defined in Fig. 27 is shown in Fig. 32a. It can be seen that the crack aperture decreases with the increase of E. Twisting angles for the 5 GPa and 50 GPa cases are 2.56° and 1.48°, respectively, which can be explained by the fact that higher fluid pressure leads to a smaller K_{III}/K_I ratio and thus a smaller twisting angle. A smaller twisting angle means a narrower gap between overlapped segments. According to the stress-based crack propagation criterion given in Section 3.3, the overlapped segments with a narrower gap are harder to propagate towards each other along the circumferential direction. Thus, it can be conjectured that a smaller twisting angle leads to lower overlapping ratios. For instance, in the base case, the overlapping ratios ω are 19.26% and 15.72% for the 5 GPa and 50 GPa cases, respectively.

5.2. Effects of fluid viscosity

In this section, two other fluid viscosities (a smaller one $\mu = 0.001$ Pa·s and a larger one $\mu = 0.1$ Pa·s) are considered, and all other parameters are kept unchanged. The parametric maps of the propagation regime are given in Fig. 30c and d, it can be found that with the increases of fluid viscosity, the propagation regime shows a variation tendency from region K to region M. The variations of injection pressure are given in Fig. 31b, in which the increasing ratios χ for cases $\mu = 0.001$ Pa·s and $\mu = 0.1$ Pa·s are 79.89% and 39.99%, respectively. It can be found that χ decreases with the increase of fluid viscosity μ. Hence, it can be concluded that, from the point of view of pressure increase degree, the influences of crack front segmentation in toughness-dominated fracturing cases are stronger than in the viscosity-dominated cases. Besides, the curve of crack aperture along the path defined in Fig. 27 is shown in Fig. 32b, from which it can be found that the crack aperture increases with increasing μ and the curve is noticeably flatter for a smaller μ. Twisting angles for the 0.001 Pa·s and 0.1 Pa·s cases are 1.82° and 1.52°, respectively, and the corresponding overlapping ratios are 17.41% and 16.13%.

5.3. Effects of fluid pumping rate

The fluid pumping rate is another important parameter in hydraulic fracturing treatment. Hence, in this section, $Q_{inj} = 0.0005$ m^3/s and 0.005 m^3/s are simulated to compare with the base case. The parametric maps of the propagation regime are given in Fig. 30e and f, it can be seen that as the fluid pumping rate increases, the propagation regime shows the tendency of transformation from toughness domination to viscosity domination. The evolutions of injection pressure with time are shown in Fig. 31c, in which the increasing ratios χ for cases $Q_{inj} = 0.0005$ m^3/s and $Q_{inj} = 0.005$ m^3/s are 49.86% and 31.75%, respectively. It can be found that χ decreases with the increase of Q_{inj}. The curve of crack aperture along the path is given in Fig. 32c, from which it can be observed that the crack aperture increases with increasing Q_{inj}. In addition, twisting

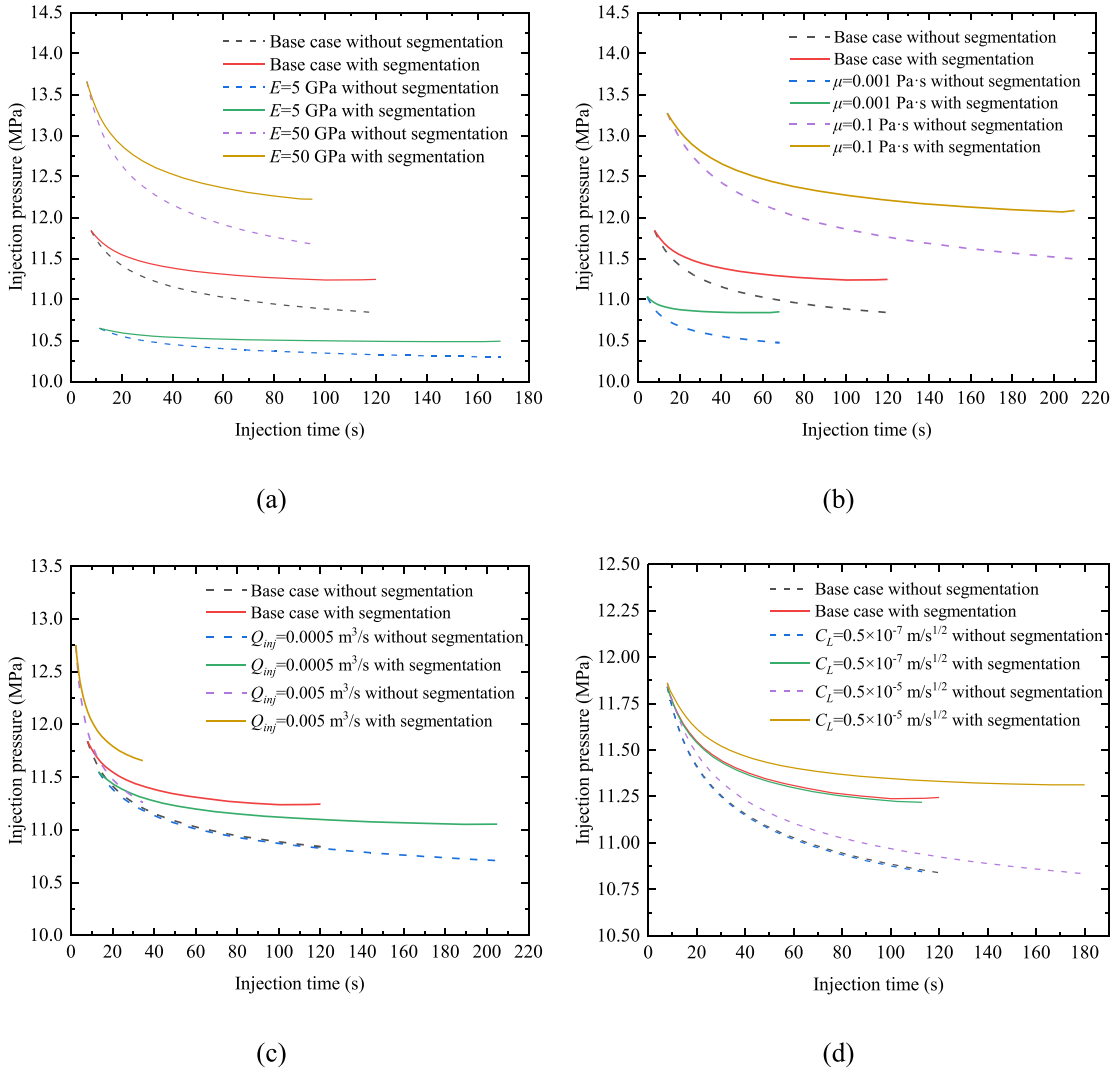

Fig. 31. Effects of elastic modulus (a), fluid viscosity (b), fluid pumping rate (c), and fluid leak-off coefficient (d) on injection pressure of segmented crack.

angles for the 0.0005 m^3/s and 0.005 m^3/s cases are 1.74° and 1.58°, respectively, and the corresponding overlapping ratios are 17.22% and 16.51%.

5.4. Effects of fluid leak-off coefficient

The effects of fluid leak-off coefficient C_L are investigated in this section by simulating the cases where $C_L = 0.5 \times 10^{-7} m/\sqrt{s}$ and $C_L = 0.5 \times 10^{-5} m/\sqrt{s}$. The parametric maps of the propagation regime are given in Fig. 30g and h, it can be noticed that as the fluid leak-off coefficient increases, the propagation regime shows a variation tendency towards the leak-off viscosity domination. The evolutions of injection pressure with time are shown in Fig. 31d and the increasing ratios of injection pressure (χ) for cases $C_L = 0.5 \times 10^{-7} m/\sqrt{s}$ and $C_L = 0.5 \times 10^{-5} m/\sqrt{s}$ are 44.14% and 57.43%, respectively. It can be noticed that χ increases with the increase of C_L. The curve of crack aperture along the path is given in Fig. 32d. It can be observed that the crack aperture decreases with increasing C_L, and C_L shows minimal impact compared to other parameters. Besides, twisting angles for the $0.5 \times 10^{-7} m/\sqrt{s}$ and $0.5 \times 10^{-5} m/\sqrt{s}$ cases are 1.71° and 1.66°, respectively, and the corresponding overlapping ratios are 17.01% and 16.86%.

The twisting angles and overlapping ratios of each case are summarized in Fig. 33a and b, respectively. It can be seen that the elastic modulus E of rock formation has the strongest influence on both the twisting angle and the overlapping ratio, followed by the fluid viscosity μ, the fluid injection rate Q_{inj}, and the fluid leak-off coefficient C_L.

6. Conclusions

The front segmentation phenomena of fluid-driven cracks under mixed loading conditions have been widely noticed in both laboratory experiments and nature. Nevertheless, it's still a very challenging task to accurately capture this complex process in numerical simulation and the available models are very limited in the literature. In this paper, a capable numerical model in light of the mesh-independence characteristic of the XFEM is proposed. The fully-coupled momentum balance equation and the fluid flow equation are solved using the Newton-Raphson method. A stress-based criterion is proposed to trace the evolution of crack surfaces. Besides, in the frame of the XFEM, a robust local mesh refinement scheme of the tip-enriched elements is implemented to effectively enhance the resolution and accuracy of the near-front stress field. Afterwards, the locally refined elements are partitioned into tetrahedra to perform numerical integration. According to the verification examples and parameter sensitivity study performed in this paper, the following conclusions can be drawn:

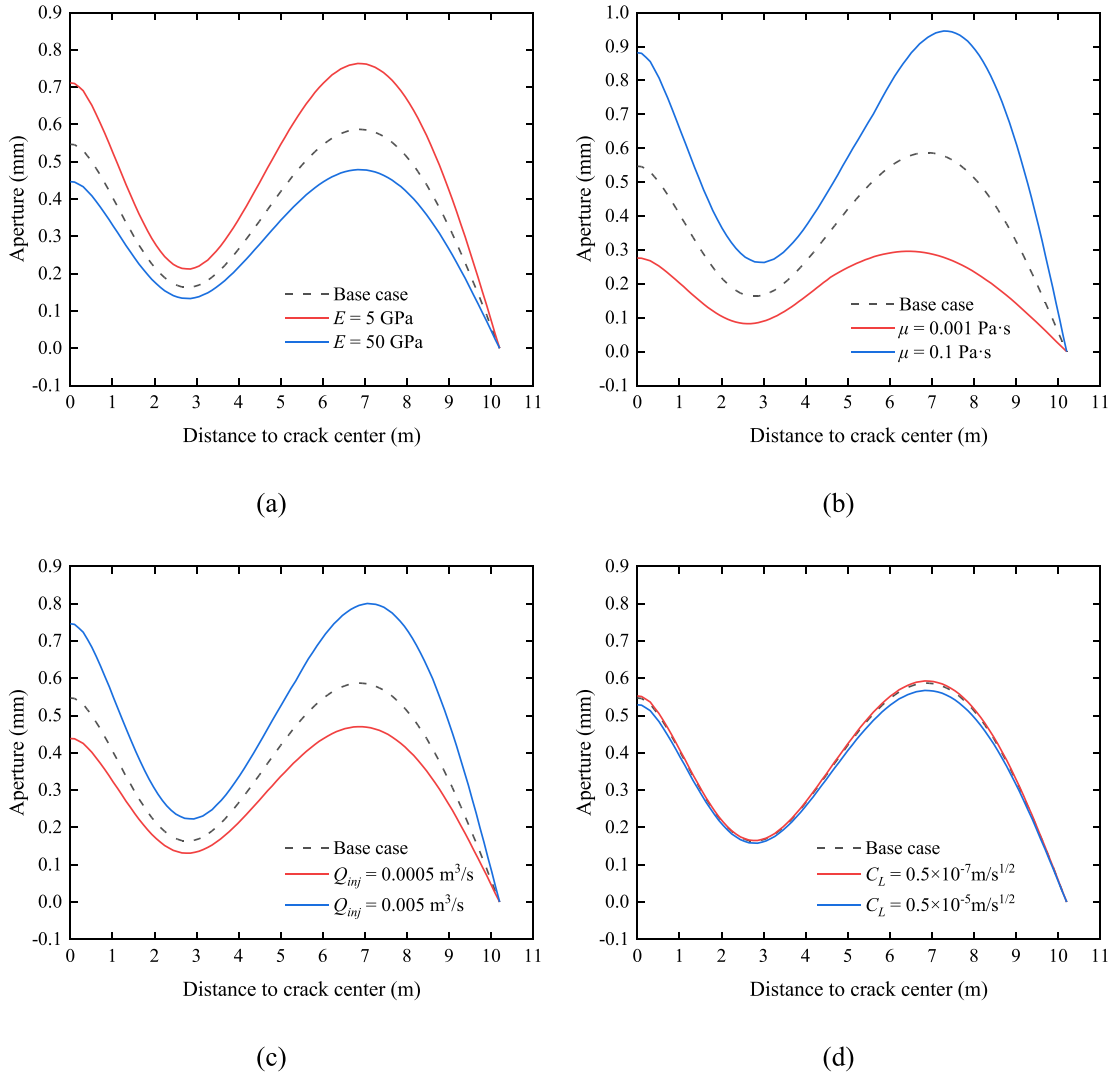

Fig. 32. Effects of elastic modulus (a), fluid viscosity (b), fluid pumping rate (c), and fluid leak-off coefficient (d) on crack apertures along the path defined in Fig. 27.

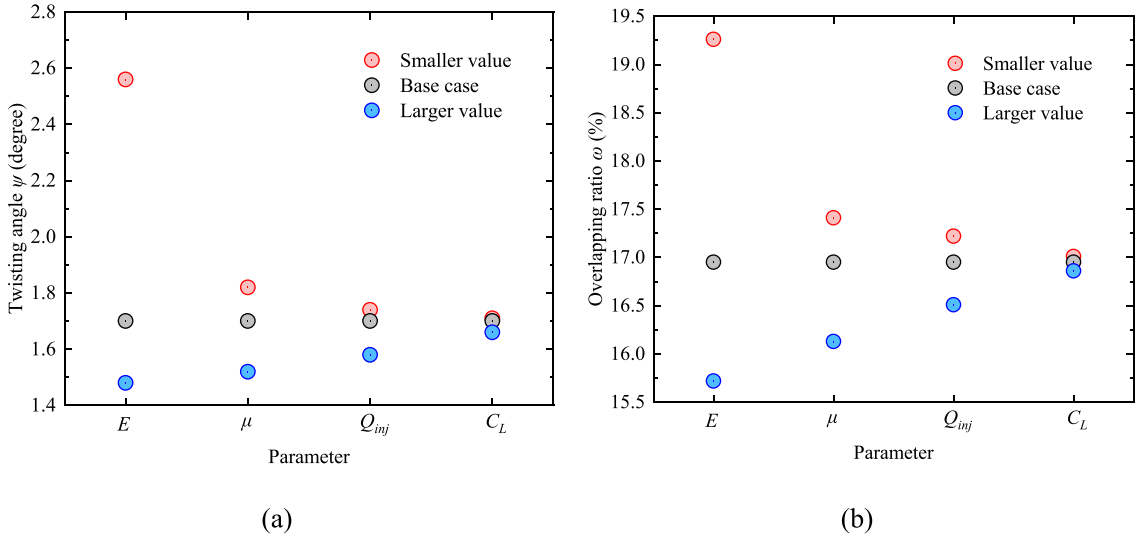

Fig. 33. Summary of twisting angles ψ (a) and overlapping ratios ω (b) obtained from the parameter sensitivity analysis.

(1) The proposed numerical strategy is capable of modeling the front segmentation process of hydraulic fractures under mixed loading conditions.
(2) Due to the mechanical interactions between overlapped segments, a higher pumping pressure is required to propagate the crack compared to the cases without considering crack front segmentation.
(3) Larger elastic modulus of rock formation, larger fluid viscosity, higher fluid pumping rate, and smaller fluid leak-off coefficient can alleviate the effects of crack front segmentation on the injection pressure.
(4) The influences of crack front segmentation on the injection pressure in toughness-dominated cases are stronger than that in viscosity-dominated cases.
(5) Larger elastic modulus, larger fluid viscosity, higher fluid pumping rate, and greater fluid leak-off coefficient lead to smaller twisting angles of the segments and smaller overlapping ratios. Besides, compared to other parameters, the fluid leak-off coefficient has a limited effect on the twisting angle and overlapping ratio.
(6) When considering crack front segmentation, chocking points of crack apertures are noticed on the paths defined along the radial direction.

Credit author statement

Fang Shi: Conceptualization, Methodology, Software, Funding acquisition. **Daobing Wang**: Validation, Data curation, Visualization, Writing-Original draft preparation. **Hong Li**: Writing- Reviewing and Editing.

Declaration of competing interest

The authors declare that they have no known competing financial interests or personal relationships that could have appeared to influence the work reported in this paper.

Acknowledgments

This work was jointly supported by the National Natural Science Foundation of China [Grant No. 51904111]; and the National Science Foundation of the Jiangsu Higher Education Institutions of China [Grant No. 19KJD430003].

References

Abass, H.H., Hedayati, S., Meadows, D.L., 1996. Nonplanar fracture propagation from a horizontal wellbore: experimental study. SPE Prod. Oper. 11 (3), 133–137.
Abelson, M., Agnon, A., 1997. Mechanics of oblique spreading and ridge segmentation. Earth Planet Sci. Lett. 148, 405–421.
Adachi, J., Siebrits, E., Peirce, A., Desroches, J., 2007. Computer simulation of hydraulic fractures. Int. J. Rock Mech. Min. Sci. 44 (5), 739–757.
Advani, S.H., Lee, J.K., 1982. Finite element model simulations associated with hydraulic fracturing. SPE-3009-PA 22 (2), 209–218.
Ahrens, T.J., 1995. Rock Physics and Phase Relations: A Handbook of Physical Constants. American Geophysical Union, Washington, D.C.
Batchelor, G.K., 1967. An Introduction to Fluid Dynamics. Cambridge University Press, Cambridge.
Baydoun, M., Fries, T.P., 2012. Crack propagation criteria in three dimensions using the XFEM and an explicit-implicit crack description. Int. J. Fract. 178, 51–70.
Belytschko, T., Black, T., 1999. Elastic crack growth in finite elements with minimal remeshing. Int. J. Numer. Methods Eng. 45, 601–620.
Biner, S.B., 2017. Programming Phase-Field Modeling. Springer, Cham, Switzerland.
Boor, C.D., 2001. A Practical Guide to Splines. Springer-Verlag, New York.
Carter, R.D., 1957. Derivation of the General Equation for Estimating the Extent of the Fractured Area, Drilhng and Production Practices. American Petroleum Institute, Dallas, pp. 261–270.
Chen, C.-H., et al., 2015. Crack front segmentation and facet coarsening in mixed-mode fracture. Phys. Rev. Lett. 115, 265503.
Citarella, R., Buchholz, F.-G., 2008. Comparison of crack growth simulation by DBEM and FEM for SEN-specimens undergoing torsion or bending loading. Eng. Fract. Mech. 75, 489–509.
Damjanac, B., Cundall, P., 2016. Application of distinct element methods to simulation of hydraulic fracturing in naturally fractured reservoirs. Comput. Geotech. 71, 283–294.
Doitrand, A., Leguillon, D., 2018. Numerical modeling of the nucleation of facets ahead of a primary crack under mode I+ III loading. Int. J. Fract. 213, 37–50.
Dong, C.Y., Pater, C.J.d., 2001. Numerical implementation of displacement discontinuity method and its application in hydraulic fracturing. Comput. Methods Appl. Math. 191, 745–760.
Dontsov, E.V., 2016. An approximate solution for a penny-shaped hydraulic fracture that accounts for fracture toughness, fluid viscosity and leak-off. R. Soc. Open Sci. 3, 160737.
Duflot, M., 2006. A meshless method with enriched weight funtions for three-dimensional crack propagation. Int. J. Numer. Methods Eng. 65, 1970–2006.
Dumstorff, P., Meschke, G., 2007. Crack propagation criteria in the framework of X-FEM-based structural analyses. Int. J. Numer. Anal. Methods GeoMech. 31, 239–259.
Economides, M.J., Martin, T., 2007. Modern Fracturing Enhancing Natural Gas Production. BJ Services Company, Houston, TX.
Fries, T.P., 2008. A corrected XFEM approximation without problems in blending elements. Int. J. Numer. Methods Eng. 75 (5), 503–532.
Fu, W., Bunger, A.P., 2019. 3D DEM Simulation on the Interference of Multiple Hydraulic Fractures in Horizontal Wells, 53rd U.S. Rock Mechanics/Geomechanics Symposium. OnePetro, New York City, New York.
Guo, J., Lu, Q., Chen, H., Wang, Z., Tang, X., Chen, L., 2018. Quantitative phase field modeling of hydraulic fracture branching in heterogeneous formation under anisotropic in-situ stress. J. Nat. Gas Sci. Eng. 56, 455–471.
Gupta, P., Duarte, C.A., 2018. Coupled hydromechanical-fracture simulations of nonplanar three-dimensional hydraulic fracture propagation. Int. J. Numer. Anal. Methods GeoMech. 42, 143–180.
Haddad, M., Sepehrnoori, K., 2016. XFEM-based CZM for the simulation of 3D multiple-cluster hydraulic fracturing in quasi-brittle shale formations. Rock Mech. Rock Eng. 49, 4731–4748.
Henry, H., 2016. Crack front instabilities under mixed mode loading in three dimensions. EPL (Europhysics Letters) 114 (6), 66001.
Huang, K., Zhang, Z., Ghassemi, A., 2013. Modeling three-dimensional hydraulic fracture propagation using virtual multidimensional internal bonds. Int. J. Numer. Anal. Methods GeoMech. 37 (13), 2021–2038.
Hubbert, M.K., Willis, D.G., 1957. Mechanics of hydraulic fracturing. J. Petrol. Technol. 9 (6), 153–168.
Jamaloei, B.Y., 2021. A critical review of common models in hydraulic-fracturing simulation: a practical guide for practitioners. Theor. Appl. Fract. Mech. 113, 102937.
Ji, L., Settari, A., Sullivan, R.B., 2009. A novel hydraulic fracturing model fully coupled with geomechanics and reservoir simulation. SPE J. 14 (4), 423–430.
Jin, W., Arson, C., 2020. Fluid-driven transition from damage to fracture in anisotropic porous media: a multi-scale XFEM approach. Acta Geotech 15, 113–144.
Khoei, A.R., Hirmand, M., Vahab, M., Bazargan, M., 2015. An enriched FEM technique for modeling hydraulically driven cohesive fracture propagation in impermeable media with frictional natural faults: numerical and experimental investigations. Int. J. Numer. Methods Eng. 104 (6), 439–468.
Knauss, W.G., 1970. An observation of crack propagation in anti-plane shear. Int. J. Fract. Mech. 6, 183–187.
Lazarus, V., Buchholz, F.G., Fulland, M., Wiebesiek, J., 2008. Comparison of predictions by mode II or mode III criteria on crack front twisting in three or four point bending experiments. Int. J. Fract. 153 (2), 141–151.
Lazarus, V., Leblond, J.-B., Mouchrif, S.-E., 2001. Crack front rotation and segmentation in mixed mode I + III or I + II + III. Part II: comparison with experiments. J. Mech. Phys. Solid. 49, 1421–1443.
Leblond, J.-B., Frelat, J., 2014. Development of fracture facets from a crack loaded in mode I+III: solution and application of a model 2D problem. J. Mech. Phys. Solid. 64, 133–153.
Leblond, J.-B., Karma, A., Lazarus, V., 2011. Theoretical analysis of crack front instability in mode I+ III. J. Mech. Phys. Solid. 59 (9), 1872–1887.
Lecampion, B., Bunger, A., Zhang, X., 2018. Numerical methods for hydraulic fracture propagation: a review of recent trends. J. Nat. Gas Sci. Eng. 49, 66–83.
Lin, B., Mear, M.E., Ravi-Chandar, K., 2010. Criterion for initiation of cracks under mixed-mode I + III loading. Int. J. Fract. 165, 175–188.
Liu, Q., Sun, L., Tang, X., Guo, B., 2019. Modelling hydraulic fracturing with a point-based approximation for the maximum principal stress criterion. Rock Mech. Rock Eng. 52, 1781–1801.
Lo, D.S.H., 2015. Finite Element Mesh Generation. CRC Press, New York.
Loehnert, S., Mueller-Hoeppe, D.S., Wriggers, P., 2011. 3D corrected XFEM approach and extension to finite deformation theory. Int. J. Numer. Methods Eng. 86, 431–452.
Mark, J.E., 2009. Polymer Data Handbook. Oxford University Press, New York, USA.
Melenk, J.M., Babuška, I., 1996. The Partition of Unity Finite Element Method: Basic Theory and Applications. Seminar fur Angewandte Mathematik, Eidgenossische Technische Hochschule, Switzerland.
Meng, C., Maerten, F., Pollard, D.D., 2013. Modeling mixed-mode fracture propagation in isotropic elastic three dimensional solid. Int. J. Fract. 179, 45–57.
Meng, C., Pollard, D.D., 2012. Modeling Mixed-Mode Fracture Propagation in 3D, 46th U.S. Rock Mechanics/Geomechanics Symposium. ARMA-2012-2179. American Rock Mechanics Association, Chicago, Illinois.
Moës, N., Dolbow, J., Belytschko, T., 1999. A finite element method for crack growth without remeshing. Int. J. Numer. Methods Eng. 46 (1), 131–150.
Moës, N., Gravouil, A., Belytschko, T., 2002. Non-planar 3D crack growth by the extended finite element and level sets, Part II: mechanical model. Int. J. Numer. Methods Eng. 53, 2549–2568.

Montgomery, C.T., Smith, M.B., 2010. Hydraulic fracturing: history of an enduring technology. J. Petrol. Technol. 62 (12), 26–40.
Ouchi, H., Katiyar, A., York, J., Foster, J.T., Sharma, M.M., 2015. A fully coupled porous flow and geomechanics model for fluid driven cracks: a peridynamics approach. Comput. Mech. 55, 561–576.
Pascau, J., Pérez, J.M.M., 2013. Image Processing with ImageJ. Packt Publishing, Birmingham, UK.
Paul, B., et al., 2018. 3D coupled HM-XFEM modeling with cohesive zone model and applications to non planar hydraulic fracture propagation and multiple hydraulic fractures interference. Comput. Methods Appl. Math. 342, 321–353.
Pereira, J.P., Duarte, C.A., Jiao, X., 2010. Three-dimensional crack growth with hp-generalized finite element and face offsetting methods. Comput. Mech. 46, 431–453.
Pham, K.H., Ravi-Chandar, K., 2014. Further examination of the criterion for crack initiation under mixed-mode I+III loading. Int. J. Fract. 189, 121–138.
Pham, K.H., Ravi-Chandar, K., 2016. On the growth of cracks under mixed-mode I+ III loading. Int. J. Fract. 199, 105–134.
Pham, K.H., Ravi-Chandar, K., 2017. The formation and growth of echelon cracks in brittle materials. Int. J. Fract. 206, 229–244.
Pollard, D.D., Segall, P., Delaney, P.T., 1982. Formation and interpretation of dilatant echelon cracks. Geol. Soc. Am. Bull. 93, 1291–1303.
Pons, A.J., Karma, A., 2010. Helical crack-front instability in mixed-mode fracture. Nature 464, 85–89.
Remij, E.W., Remmers, J.J.C., Pizzocolo, F., Smeulders, D.M.J., Huyghe, J.M., 2015. A partition of unity-based model for crack nucleation and propagation in porous media, including orthotropic materials. Transport Porous Media 106, 505–522.
Rivas, E., Gracie, R., 2020. A monolithic coupled hydraulic fracture model with proppant transport. Comput. Methods Appl. Math. 372, 113361.
Shi, F., Liu, J., 2021. A fully coupled hydromechanical XFEM model for the simulation of 3D non-planar fluid-driven fracture propagation. Comput. Geotech. 132, 103971.
Shi, F., Wang, D., Chen, X., 2021. A numerical study on the propagation mechanisms of hydraulic fractures in fracture-cavity carbonate reservoirs. Comput. Model. Eng. Sci. 127, 015384.
Shi, F., Wang, D., QuanquanYang, 2022. An XFEM-based numerical strategy to model three-dimensional fracture propagation regarding crack front segmentation. Theor. Appl. Fract. Mech. 118, 103250.
Shi, F., Wang, X., Liu, C., Liu, H., Wu, H., 2016. A coupled extended finite element approach for modeling hydraulic fracturing in consideration of proppant. J. Nat. Gas Sci. Eng. 33, 885–897.
Shi, F., Wang, X., Liu, C., Liu, H., Wu, H., 2017. An XFEM-based method with reduction technique for modeling hydraulic fracture propagation in formations containing frictional natural fractures. Eng. Fract. Mech. 173, 64–90.
Smith, I.M., Griffiths, D.V., Margetts, L., 2014. Programming the Finite Element Method. John Wiley & Sons, West Sussex, United Kingdom.
Sommer, E., 1969. Formation of fracture 'lances' in glass. Eng. Fract. Mech. 1 (3), 539–546.
Sun, L., Zhao, G., Ma, X., 2012. Adaptive generation and local refinement methods of three-dimensional hexahedral element mesh. Finite Elem. Anal. Des. 50, 184–200.
Tada, H., Paris, P.C., Irwin, G.R., 2000. Stress Analysis of Cracks Handbook. ASME Press, New York.
Tian, R., Wen, L., Wang, L., 2019. Three-dimensional improved XFEM (IXFEM) for static crack problems. Comput. Methods Appl. Math. 343, 339–367.
Wang, D., Shi, F., Hao, Q., 2021. Failure patterns and mechanisms of hydraulic fracture propagation behavior in the presence of naturally cemented fractures. Comput. Model. Eng. Sci. 127, 014206.
Wolff, K.P., Pitangueira, R.L.S., Peixoto, R.G., 2020. A displacement-based and explicit non-planar 3D crack propagation model in the generalized/extended finite element method. Theor. Appl. Fract. Mech. 108, 102647.
Wu, R., Germanovich, L.N., Hurt, R.S., 2009. Experimental and Theoretical Study of Mixed-Mode I+III Crack Propagation and Segmentation, 43rd U.S. Rock Mechanics Symposium & 4th U.S. - Canada Rock Mechanics Symposium. American Rock Mechanics Association, Asheville, North Carolina.
Xiao, G., Wen, L., Tian, R., 2021. Arbitrary 3D crack propagation with Improved XFEM: accurate and efficient crack geometries. Comput. Methods Appl. Math. 377, 113659.
Younes, A.I., Engelder, T., 1999. Fringe cracks: key structures for the interpretation of the progressive Alleghanian deformation of the Appalachian plateau. GSA Bulletin 111 (2), 219–239.